ACS OMEGA

http://pubs.acs.org/journal/acsodf

Article

Crystal Plane Impact of $ZnFe_2O_4$–Ag Nanoparticles Influencing Photocatalytical and Antibacterial Properties: Experimental and Theoretical Studies

Carlos Alberto Huerta-Aguilar, Zarick Juliana Diaz-Puerto, Eduardo Daniel Tecuapa-Flores, and Pandiyan Thangarasu*

Cite This: *ACS Omega* 2022, 7, 33985–34001

Read Online

ACCESS | Metrics & More | Article Recommendations | Supporting Information

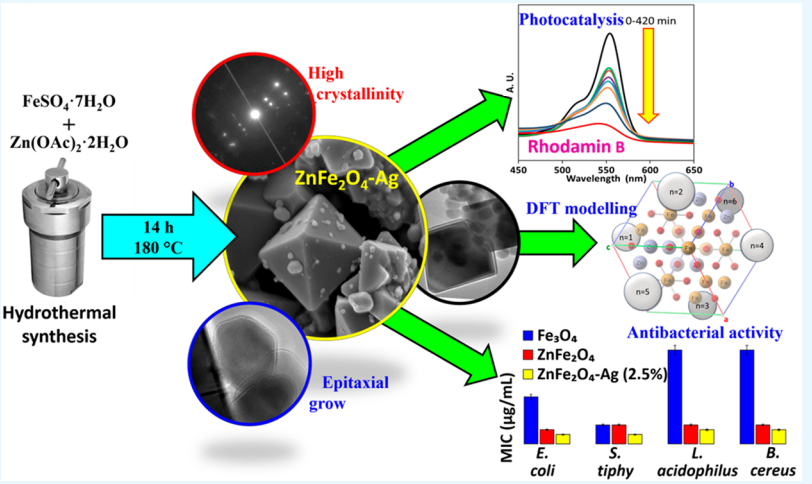

ABSTRACT: This paper describes the crystal interphase impact of $ZnFe_2O_4$–Ag in the photodegradation of Rhodamine B. Prepared $ZnFe_2O_4$ nanoparticles (NPs) were deposited with Ag NPs to offer $ZnFe_2O_4$–Ag (0–2.5%). An X-ray diffraction peak corresponding to the Ag NPs was detected if the particle content reached about 2.0%, observing multiple crystalline interphases in HR-TEM. Magnetic saturation (Ms) was increased ∼160% times for $ZnFe_2O_4$–Ag (7.25 to 18.71 emu/g) and $ZnFe_2O_4$ (9.62 to 25.09 emu/g) if the temperature is lowered from 298 to 5.0 K; while for Fe_3O_4 (91.09 to 96.19 emu/g), the Ms increment was just about 5.6%. After analyzing the DFT–Density of State, a decrease of bandgap energy for $ZnFe_2O_4$–Ag_6 from the influence of the size of Ag cluster was seen. Quantum yield (Φ) was 0.60 for $ZnFe_2O_4$, 0.25 for $ZnFe_2O_4$–Ag (1.0%), 0.70 for $ZnFe_2O_4$–Ag (1.5%), 0.66 for $ZnFe_2O_4$–Ag (2.0%), and 0.66 for $ZnFe_2O_4$–Ag (2.5%), showing that the disposition of Ag NPs (1.5–2.5%) increases the Φ to >0.60. The samples were used to photo-oxidize RhB under visible light assisted by photopowered Langmuir adsorption. The degradation follows first-order kinetics ($k = 5.5 \times 10^{-3}$ min^{-1}), resulting in a greater $k = 2.0 \times 10^{-3}$ min^{-1} for $ZnFe_2O_4$–Ag than for $ZnFe_2O_4$ (or Fe_3O_4, $k = 1.1 \times 10^{-3}$ min^{-1}). DFT-total energy was used to analyze the intermediates formed from the RhB oxidation. Finally, the $ZnFe_2O_4$–Ag exhibits good antibacterial behavior because of the presence of Zn and the Ag components.

INTRODUCTION

The study of iron oxides (Fe_2O_3 and Fe_3O_4) is a growing research topic because of their good superparamagnetic behavior and suitable biocompatibility in several biological applications such as cell imaging and drug delivery.[1] As is known, the factors like size, crystalline nature, internal structural texture, and unbalanced surface spins significantly influence the magnetic properties. Nonetheless, the air sensitivity of iron oxides is one of the main obstacles to its use as it tends to react quickly with water or acids; moreover, if Fe_3O_4 NPs are present in the solution, the aggregation of the particles is extremely quick due to the high magnetic nature.[2] It is known that nanoparticles (size, 1.0–100 nm) behave exceptionally because of the quantum confinement effect, and reveal unique electronic, magnetic, and optical properties.[3] The improvement of the above properties can be achieved if

Received: May 20, 2022
Accepted: August 29, 2022
Published: September 16, 2022

the iron oxide is doped or deposited by different metals i.e., MFe_2O_4 (M = Mn, Co, Ni, Zn, Mg, etc.). Thus, a high magnetization saturation was obtained for $MnFe_2O_4$ NPs, while for $CoFe_2O_4$ NPs, a hard-magnet property is observed as compared to Fe_3O_4.[4] This means that the structural change in the two cation centers $\{(M^{2+}_{1-c}Fe_c^{3+})_A[M_c^{2+}\ Fe_{2-c}^{3+}]_BO_4$ (c = inversion parameter) impacts significantly the electronic and magnetic properties. The distribution degree in the inversion character (i.e., occupational disorder factor c) influences the fractional number, improving the magnetic and catalytic properties.[5] This means that the structural change in the zinc ferrites can trap electrons inside the quasi-stable energy states (active sites) to reduce the recombination effect (e^-/h^+).

Although a narrow band gap energy (E_g = 1.92 eV) was obtained for $ZnFe_2O_4$, supporting visible light absorption,[6,7] it suffers largely from a high recombination effect, affecting the photocatalytic efficiency.[7] This is the reason why the ferrite system has to be modified to use as effective photocatalysts.[8]

Namely, the electrochemical potential of the valence band (VB) is estimated to be 0.38 V for $ZnFe_2O_4$, while for its conduction band (CB), it has been determined to be −1.54 V vs NHE.[6] There are several reports on MFe_2O_4 (M = Mn, Co, Ni, Zn, Mg, etc.); however, $ZnFe_2O_4$ is more interesting for the geometrical change associated with electronic, magnetic, and catalytic properties. Zn^{2+} ions prefer to occupy a tetrahedral geometry in the spinel structure $\{(M^{2+}_{1-c}Fe_c^{3+})_A[M_c^{2+}\ Fe_{2-c}^{3+}]_BO_4$ (c = inversion parameter) impacting significantly the electronic, magnetic, and catalytic behaviors.[9] $ZnFe_2O_4$ exhibits an antiferromagnetic property at low temperature (10 K) in a normal spinel structure, but it behaves in a paramagnetic nature at room temperature. This occurs because Zn^{2+} (nonmagnetic) occupies strongly at tetrahedral A sites, forcing all Fe^{3+} ions to reside in the octahedral B sites, and as a result, the negative superexchange interaction among the Fe^{3+} in the octahedral occurs leading to antiferromagnetism at low temperature. For the nanosize of $ZnFe_2O_4$, a ferromagnetic order was seen even at room temperature due to the redistribution of cations between both A and B sites, where some Zn^{2+} ions (positioned in A site) are transferred to B site, in the same way, some of Fe^{3+} (B site) has been moved to A site. These movements impact considerably on the electronic, magnetic, and catalytic characteristics. Zn^{2+} ion is nontoxic, and a biologically essential element, exhibiting a narrow band gap energy (E_g = 1.92 eV), which favors visible light absorption. Furthermore, the spinel structure of $ZnFe_2O_4$ gives additional catalytic sites by virtue of the crystal lattice enhancing the photodegradation capabilities. The electronic inert nature of Zn^{2+} (d^{10} configuration) offers high photochemical stability for $ZnFe_2O_4$, giving the advantage for the recovery and reuse in the photodegradation. $ZnFe_2O_4$−Ag (2.5%) performs as an effective photocatalyst since Ag NPs can absorb visible light because of the SPR effect, inducing the flow of plasmon electrons from Ag NPs to the CB of $ZnFe_2O_4$. As a result, the charge separation can be enhanced. At the same time, a portion of the CB electrons of $ZnFe_2O_4$ can be shifted toward the Ag^+ ions, reducing some Ag^+ ions to Ag NPs; in addition, it has been shown to be an antibacterial agent more than other elements. So, the present work is focused on the deposition of Ag NPs on $ZnFe_2O_4$ at different proportions, and the influence of electronic and magnetic properties on the photocatalytic and antibacterial behavior was analyzed. Comprehensively, for $ZnFe_2O_4$−Ag NPs, the band gap energy determined by diffuse reflectance spectra (DRS) is corroborated with that derived from DFT-density of states (DOS). To the best of our knowledge, the theoretical and experimental studies of $ZnFe_2O_4$−Ag have not been reported in the literature. The photocatalytic performance of $ZnFe_2O_4$−Ag NPs was also studied for RhB and phenol oxidations as the former can act as photosensitizer. The visible light-powered $ZnFe_2O_4$−Ag (2.5%) favored the RhB-adsorption (Langmuir isotherm model) and then it involved the degradation. Furthermore, the intermediate formation from the RhB oxidation was analyzed by the DFT total energy calculation.

RESULTS AND DISCUSSION

X-ray Diffraction. All the samples were analyzed by powder X-ray diffraction (PXRD) using Cu Kα radiation at 2θ in the range of 20°−80° (see Figure 1, Table S1), and

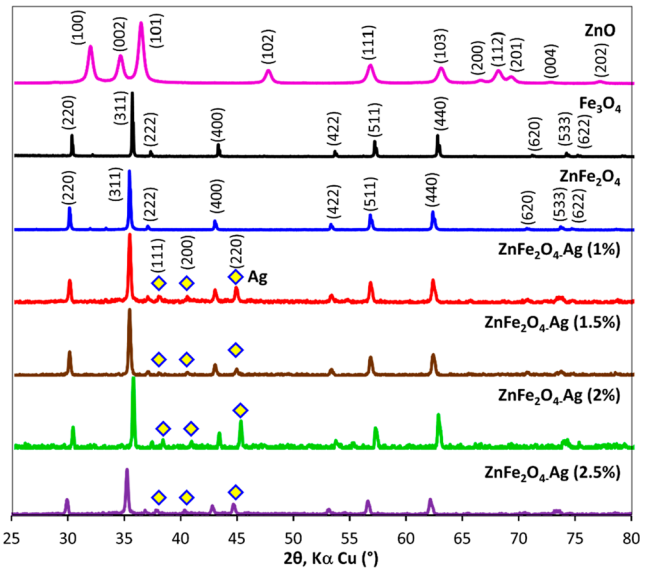

Figure 1. XRD analysis of zinc ferrites.

compared to those reported in crystallographic data index No. 0002576F AMCSD (American Mineralogist Crystal Structure Database). The crystalline parameters such as $a = b = c$ = 8.3515 Å obtained for both $ZnFe_2O_4$ and $ZnFe_2O_4$−Ag coincided with the cubic phase (JCPDS Card No. 89-1010, and JCPDS 19-0629 for Fe_3O_4). Because the peaks originating from spinel $ZnFe_2O_4$ at 2θ are 30.0, 35.00, 37.00, 43.00, 53.00, 57.00, and 62.00, representing the crystal planes of [220], [311], [222], [400], [422], [511], and [440], respectively,[10] observing a clean diffraction pattern without additional peaks, it confirms the existence of a single-phase structure of *fcc* with *Fd3m*,[11] where Zn^{2+} is occupied both octahedral and tetrahedral sites, and Fe^{2+} is located at the tetrahedral geometry (Table S2). In the formation of zinc ferrites, a partial quenching of the peak intensity (100) corresponding to ZnO was detected during the addition of Fe^{3+} at different concentrations. If the ratio of Fe^{3+} ions was increased, the peaks turned to be sharper with high intensity related to the crystallinity of $ZnFe_2O_4$ NPs. The major lattice planes (100), (002), and (101) originating from ZnO are shifted as observed from the position of I_{max} of the diffraction signal. This phenomenon can be explained since the formation of $ZnFe_2O_4$ (without incorporation of Fe^{3+}) that shifts signals to higher angles as the ionic radius of Zn^{2+} (0.074 nm) is greater than

https://doi.org/10.1021/acsomega.2c03153
ACS Omega 2022, 7, 33985−34001

that of Fe^{3+} (0.064 nm). The crystallite size calculated by the Debye−Scherrer's equation is almost the same as 35.46 nm for Fe_3O_4, 35.22 nm for $ZnFe_2O_4$, and 35.23 nm for $ZnFe_2O_4$−Ag (2.5%) NPs. Typically, the high peak intensity (311) at 35.0° is characterized as a good degree of crystallinity; yet, a small peak shift observed for $ZnFe_2O_4$−Ag (2%) was due to the influence of Ag in the crystalline phase. For example, the crystalline peaks are shifted in the right direction by the presence of a strained lattice. The compositional change in the sample would certainly influence the cell dimensions; as a result, the peak has been shifted in the right direction. Generally, the residual stress shifts the peaks in one direction, as it is required to balance at grain boundaries to satisfy the constraint strain tensor. This means that the tensile stress has been compensated by the compressive stress as the peak shift is associated with the *hkl* parameters.

In the spinel Fe_3O_4 ($Fe^{3+}{}_{Td}\ Fe^{3+}Fe^{2+}{}_{Oh}O_4$) or in the inverse spinel like Fe_3O_4 (Fe^{3+}(A) Fe^{2+} Fe^{3+}(B)O_4·) (A site, Fe^{3+} with d^5 high-spin; B site, Fe^{3+} with d^5 high-spin and Fe^{2+} with d^6 high-spin), the substitution of Fe^{3+} in the B-site by other metal ions causes a structural change, improving the electrical and magnetic properties. In the case of $ZnFe_2O_4$, the Fe^{3+} ion is occupied in an octahedral geometry, while both Fe^{2+} and Zn^{2+} ions are shared competitively in a tetrahedral geometry. Some of the Fe^{2+} ions have been replaced by Zn^{2+} in the tetrahedral sites due to its suitable electronic configuration. This observation is consistent with the previous studies that the occupation of Zn^{2+} in both tetrahedral and octahedral sites was proven by the X-ray-absorption fine structure (EXAFS).[12]

Fourier Transform Infrared (FT-IR) Spectra. FT-IR spectra (4000 and 400 cm^{-1}, Figure S1) were recorded for the samples and the vibrational signals were analyzed. Metal-O stretching primarily originated from the different distances that result in Fe^{3+}−O^{2-}, as the metal ion is occupied in both octahedral and tetrahedral sites. Thus, a typical vibrational peak (≈480 cm^{-1}) from the Zn_{Oh}−O−Fe bond (octahedral Zn ion), and another peak (≈660 cm^{-1}) from its tetrahedral position are observed as reported.[13,14] The Zn−O bonding in Zn−O−Fe, namely, 590 cm^{-1} (ν_1, M_{tetra}−O) and 418 cm^{-1} (ν_2, M_{octa}−O) corresponding to tetrahedral and octahedral Zn−O vibrations was observed, respectively. In addition, a minor peak splitting between 1600 and 800 cm^{-1} was noticed for Zn−O−Fe (bond-stretching) and establishes the existence of the tetrahedral building units.[15] Moreover, Zn^{2+} is preferred to localize in the tetrahedral sites than in other sites, forming a covalent bond through the sp^3 hybridization. Nonetheless, other signals like ≈1100 cm^1 and 1200 cm^{-1} appeared for the metal sulfate which was used for the preparation of zinc ferrite. Similarly, the peaks (2924 and 2851 cm^{-1}) indicate the presence of $ZnFe_2O_4$−Ag (2.5%) even though the signal corresponding to Ag NPs has not been detected because of its small amount in zinc ferrite. The present results are corroborated with other compounds like $NiFe_2O_4$, $CoFe_2O_4$, and $ZnFe_2O_4$, observing two typical bands, one at high-frequency (600−550 cm^{-1}) corresponding to tetrahedral and another at low-frequency peak (450−400 cm^{-1}) representing the octahedral sites.[16] The signals at 592 cm^{-1} (Ni^{2+}-O) for $NiFe_2O_4$, 572 cm^{-1} (Co^{2+}-O) for $CoFe_2O_4$, and 546 cm^{-1} (Zn^{2+}-O) for $ZnFe_2O_4$ grow from the tetrahedral sites,[17] while the peaks such as 446, 452, and 438 cm^{-1} corresponding to the respective metal ions originate from the octahedral sites.[18] Commonly, the appearance of bands around 1090 and 1600 cm^{-1} can be characterized as O−H bonds (adsorbed H_2O).

SEM Analysis. TEM and SEM analyses were performed and the morphological characteristics of the samples (facets 100 and 111, Figure 2) were studied. The results show the presence of an octahedral morphology for $ZnFe_2O_4$ NPs, consistent with the previous studies.[19] The deposition of Ag NPs on $ZnFe_2O_4$ has been seen clearly in the SEM images, and distributed randomly on the surface.

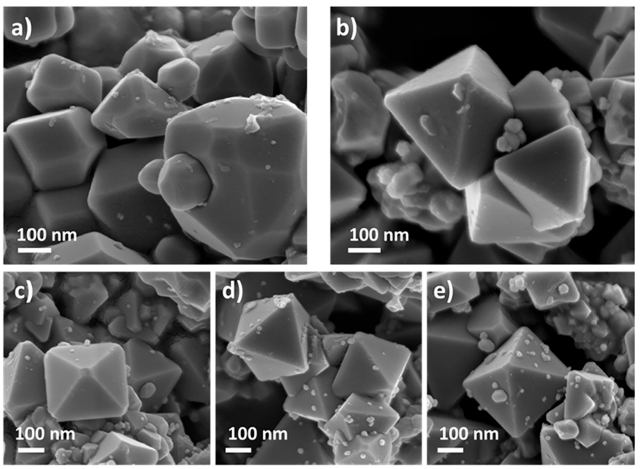

Figure 2. Scanning electron microscopy (SEM) analysis: (a) Fe_3O_4, (b) $ZnFe_2O_4$, (c) $ZnFe_2O_4$−Ag (1.0%), (d) $ZnFe_2O_4$−Ag (2.0%), and (e) $ZnFe_2O_4$−Ag (2.5%).

A few Ag NPs are dispersed on the surface of $ZnFe_2O_4$ if the Ag content is low (1.0%) (Figure 2c−e); in contrast, a greater distribution of Ag NPs was observed for the higher content of 2.5%. The particle size determined by SEM images is approximately consistent with those estimated by XRD.

TEM and HRTEM Studies. The size and morphology of Fe_3O_4, $ZnFe_2O_4$, and $ZnFe_2O_4$−Ag NPs were also studied by TEM (Figure 3), observing octahedral cubic structure for $ZnFe_2O_4$ NPs. The size of Ag NPs on the surface of zinc ferrite is found to be ∼16−25 nm, suggesting that nonmagnetic Ag NPs are offered the smallest size (10 to 15 nm) and distributed randomly in the $ZnFe_2O_4$ as observed in the SEM. Yet, the size of $ZnFe_2O_4$ NPs (70−80 nm) and Fe_3O_4 NPs (∼120 nm) is relatively greater because of their magnetic properties which encourage particle agglomeration (Figure 3a,b). Since the metal oxide acts as a nucleation center, it controls the size of Ag deposition (average size, ∼25 nm, Figure 3c,d), and also it alters the epitaxial growth of Ag atoms on the $ZnFe_2O_4$ surface. Furthermore, with the EDS analysis (Table S3), the elemental composition of the samples was determined, and the results reveal the existence of Zn, Fe, Ag, and O. The elemental percentage is nearly close to the theoretical values.[20] The atomic ratio for Fe/Zn resulted to be 2.13 for $ZnFe_2O_4$ and 2.36 for $ZnFe_2O_4$−Ag (2.5%); however, the latter ratio is slightly greater than the former because of the existence of Ag NPs.

In the HR-TEM image (Figure 3), the round-shaped Ag NPs (>20 nm) are dispersed over $ZnFe_2O_4$, giving a high crystallinity for $ZnFe_2O_4$−Ag NPs (Figure 3e) that can improve the electronic and catalytic properties.[13,21] Predominantly, $ZnFe_2O_4$ presents in the *fcc* cubic octahedral structure, where the *d*- spacing has resulted to 4.36 Å and 0.298 nm in the lattice fringes for the plane (111) and (220), respectively, agreeing with the previous report.[22] The presence of crystal

https://doi.org/10.1021/acsomega.2c03153
ACS Omega 2022, 7, 33985−34001

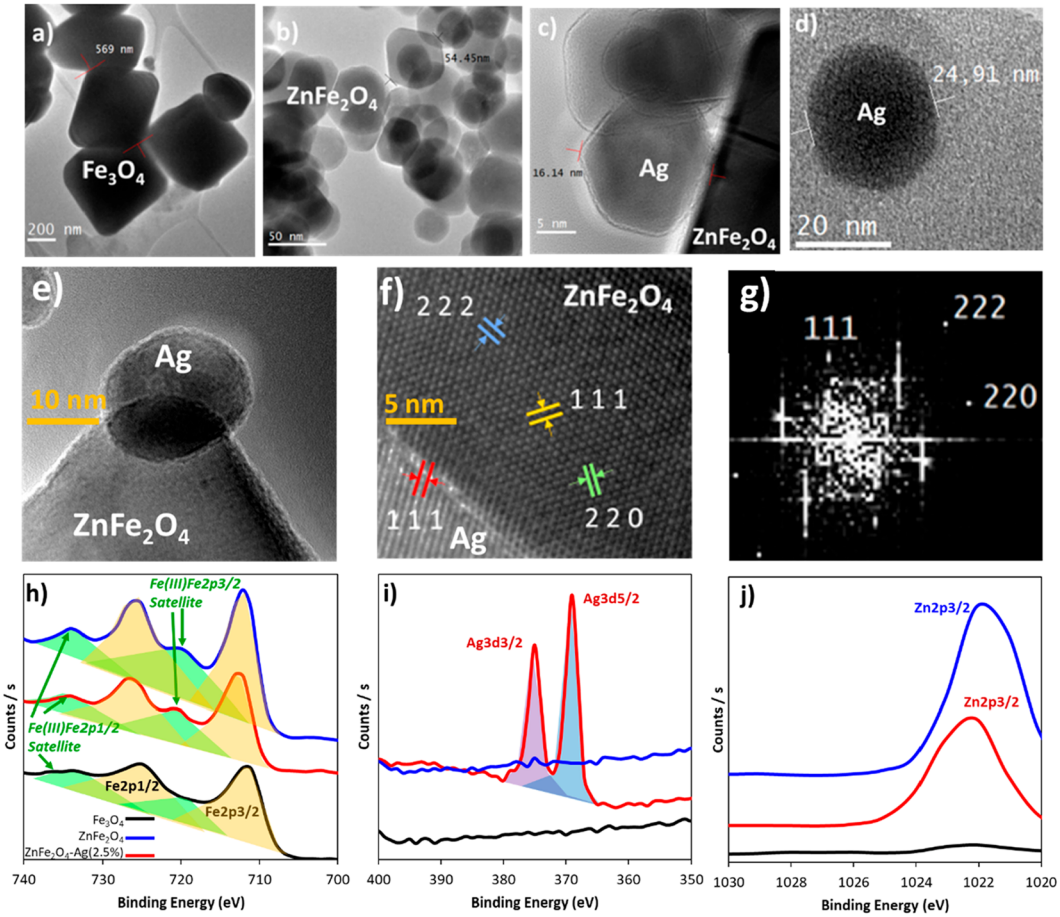

Figure 3. TEM in darkfield for zinc ferrites (top): (a) Fe_3O_4, (b) $ZnFe_2O_4$ NPs, and (c) $ZnFe_2O_4$–Ag NPs, and (d) Ag NPs. HR-TEM (middle): (e) $ZnFe_2O_4$–Ag interface and (f) FFT for HR-TEM of $ZnFe_2O_4$. (g) Lattice indexation of $ZnFe_2O_4$–Ag interface. XPS (bottom): (h) Fe 2p; (i) Ag 3d; (j) Zn 2p.

Table 1. XPS Data of the Nanocomposites

	$ZnFe_2O_4$–Ag(2.5%)		$ZnFe_2O_4$		Fe_3O_4	
Transition	E_B (eV)	fwhm	E_B (eV)	fwhm	E_B (eV)	fwhm
Zn 2p1/2	1044.08	3.2	1045.03	1.54	-	-
Zn 2p3/2	1022.08	1.0	1022.08	1.02	-	-
Fe 2p1/2	725.08	2.9	726.08	3.7	725.08	3.9
Fe 2p3/2	711.08	5.3	712.08	4.1	711.08	4.3
Fe(II)Fe 2p1/2 Satellite	-	-	-	-	736.08	5.0
Fe(III)Fe 2p1/2 Satellite	734.08	3.4	733.08	3.1	733.08	2.4
O 1s	530.08	2.62	531.08	3.21	531.08	3.17
Ag 3d3/2	375.08	2.43	-	-	-	-
Ag 3d5/2	369.08	2.11	-	-	-	-

planes (222), (111), and (220) are also seen in the $ZnFe_2O_4$–Ag NPs by the existence of spinel-type structures. The Ag atom is positioned in the vicinity of the zinc ferrite plane (020) (Figure 3f), showing its interaction with metal oxide. This implies that the interface of zinc ferrite dictates the Ag nucleation at the preferential crystalline plane (111) to offer a directional epitaxial growth for $ZnFe_2O_4$–Ag NPs. The higher degree angle was seen for $ZnFe_2O_4$–Ag NPs due to a relatively greater ionic radius of Zn^{2+} (0.074 nm) than for Fe^{3+} (0.064 nm).[23]

X-ray Photoelectron-Spectroscopy (XPS). XPS was carried out for the ferrite samples to confirm the oxidation state of metal ions Fe^{2+}, Fe^{3+}, Zn^{2+}, and Ag^0 (see Table 1, Figure S2), showing the existence of peaks corresponding to Zn, Fe, Ag, and O for $ZnFe_2O_4$–Ag NPs (Figure 3h–j). In particular, two signature peaks (1022.08 eV, fwhm = 4.36 eV for Zn $2p_{3/2}$ and ~1044 eV, fwhm = 3.21 eV for Zn $2p_{1/2}$) representing Zn species are detected; the first signal at 1022.08 eV originates from Zn^{2+} that is located in the tetrahedral A sites, while the later signal emerges from Zn^{2+} occupying the octahedral B sites.[24,25] This means that Zn^{2+} is present in both A and B sites within the ferrite crystal. In the spectra, the range 730–705 eV is assigned to Fe 2p, especially, two typical signals (~711 eV for Fe $2p_{3/2}$ from Fe^{2+} and ~725 eV for $2p_{1/2}$ from Fe^{3+}) and the energy difference between those peaks (14.0 eV)[26] confirm the presence of Fe_3O_4 in $ZnFe_2O_4$ matrix. The

https://doi.org/10.1021/acsomega.2c03153
ACS Omega 2022, 7, 33985−34001

Table 2. Magnetic Parameters of Ferrite Samples

	T = 298 K				T = 5 K			
material	Ms emu/g	Mr	SQ	Hc kOe	Ms emu/g	Mr	SQ	Hc kOe
Fe_3O_4	91.09	5.02	0.055	0.21	96.19	6.01	0.062	0.13
$ZnFe_2O_4$	9.62	0.52	0.054	0.14	25.09	4.67	0.186	0.46
$ZnFe_2O_4$–Ag(2.5%)	7.25	0.06	0.008	0.13	18.71	3.71	0.198	0.46

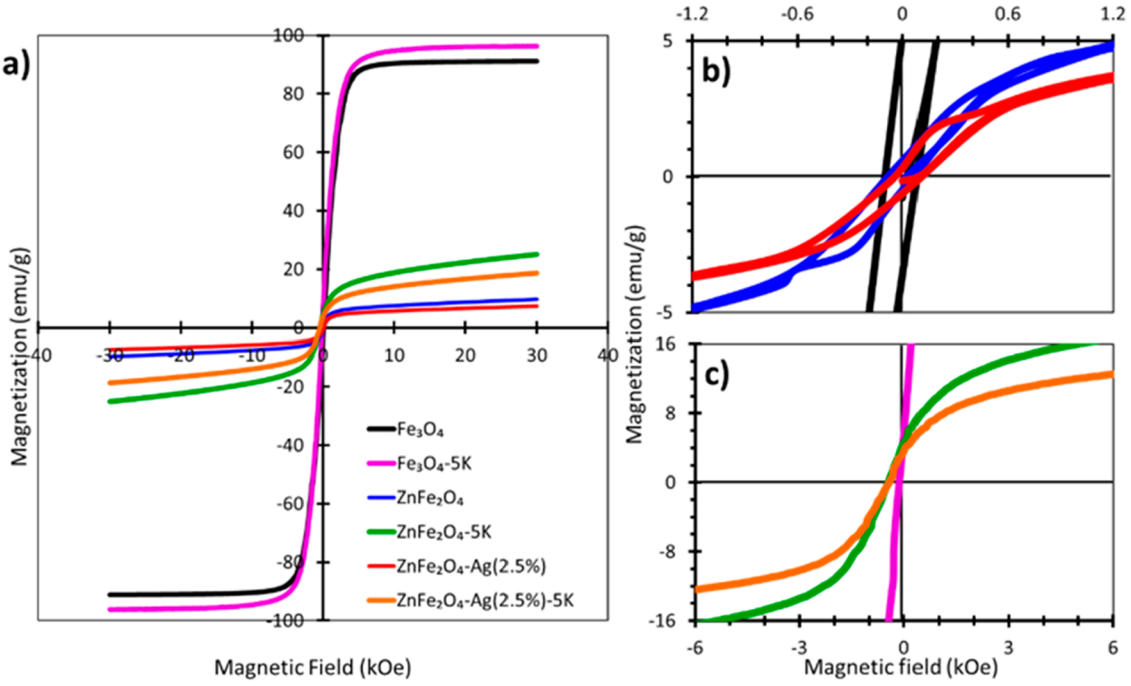

Figure 4. Magnetic properties: (a) full VSM spectra; (b) VSM intersection at 298 K, and (c) VSM at 5K.

Fe $2p_{3/2}$ signal can be deconvoluted into two peaks (712.08 and 711.08 eV) assigned to Fe^{3+} in the octahedral and tetrahedral geometry, respectively. Moreover, the satellite peak appearing around 725 eV between Fe $2p_{3/2}$ and $2p_{1/2}$ suggests the absence of the Fe_3O_4 phase in the composite. The peak originating from Fe $2p_{3/2}$ is also fitted into two peaks (~711.08 and ~710.0 eV), indicating Fe^{3+} is presented in both tetrahedral (A site) and octahedral (B sites) for $ZnFe_2O_4$. This shows that the $ZnFe_2O_4$ is presented in a partially inverse spinel structure, offering a mixture of two oxidation states (Fe^{2+} and Fe^{3+}) in contrast to Fe^{3+} in Fe_2O_3.[27] The binding energy observed for Fe $2p_{3/2}$ (712.08 and 711.08 eV) is consistent with its tetrahedral (A site) and octahedral (B site) structures, respectively. Another signal detected at 530.08 eV represents the O atom associated with the bonding of Fe^{3+} to O (Fe^{3+}–O). A broad peak ~530.08 eV corresponds to O 1s and is fitted into three peaks (~528.0, 529.0, and 531.0 eV) assigned to the lattice oxygen O^{2-} from Zn–O and Fe–O linkages. The other two peaks (531.0 and 530.0 eV) are characterized as the surface-absorbed oxygen. The peaks of Ag $3d_{5/2}$ and Ag $3d_{3/2}$ (369 and 375 eV) correspond to the Ag^0 atoms present in $ZnFe_2O_4$–Ag. However, the broadening of the Ag-peak is highly related to the Ag cluster epitaxial growth on the metal oxide. The high electronegativity of Ag (χ = 2.4) facilitates the interaction between the Ag atom and ferrite, promoting its epitaxial growth on $ZnFe_2O_4$. Thus, the electronic transfer can occur from the conduction band (CB) to Ag NPs in the $ZnFe_2O_4$ array.[28] Some minor peaks associated with impurities corresponding to Na, C, and N as sodium citrate and sodium bicarbonate were used for the preparations of Ag NPs and zinc ferrite, despite the possibility of the XPS chamber contamination (Table S4).

Magnetic Studies. The magnetic properties of the samples were analyzed on a Vibrating sample magnetometer (VSM) by applying the external magnetic fields at 298 and 5.0 K. In an isothermal magnetization (M-H), by plotting of magnetization (M) against the applied magnetic field (H), hysteresis loops were obtained; This reveals the formation of a single domain in the randomly oriented uniaxial spherical particles.[29] Since the magnetic values are highly dependent on size, the nature of morphology, and composition of the samples, a lowest magnetic saturation (Ms, 7.25 emu/g) was observed for $ZnFe_2O_4$–Ag than for $ZnFe_2O_4$ (Ms, 9.61 emu/g). For magnetite (Fe_3O_4), as anticipated, the value was greater than that observed for other samples (91.10 emu/g, see Table 2, Figure 4). However, the Ms value was increased if the temperature was lowered from 298 to 5.0 K for $ZnFe_2O_4$–Ag (7.25 to 18.71 emu/g), an increase of about 160% times greater than that observed at room temperature. The same behavior was observed for $ZnFe_2O_4$ (9.62 to 25.09 emu/g). While for Fe_3O_4, the increase was found to be just 5.0% (91.09 to 96.19 emu/g). This means that the magnetization of both $ZnFe_2O_4$ and $ZnFe_2O_4$–Ag is highly temperature sensitive, agreeing with the squareness ratio (SQ) and Hc values. For

https://doi.org/10.1021/acsomega.2c03153
ACS Omega 2022, 7, 33985−34001

Scheme 1. (a) Proposed Mechanism for the RhB Oxidation, (b) Radical Formation Detected by EPR

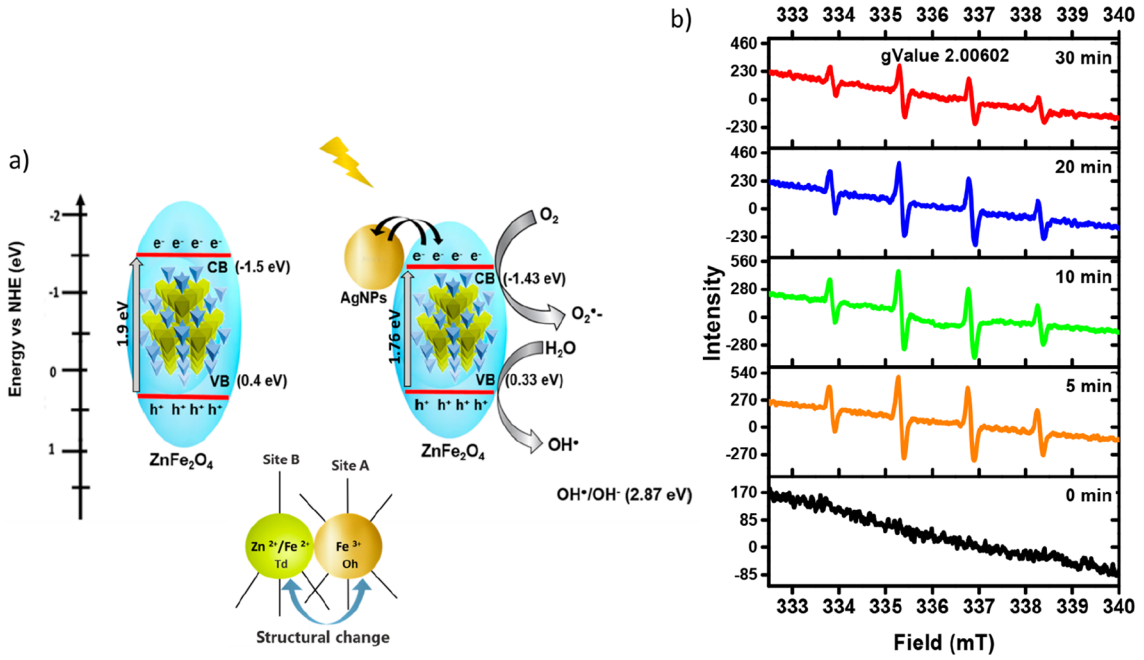

example, the squareness ratio (SQ = Mr/Ms), which is associated with the randomly oriented-uniaxial grains (small single-domain particles), results to a smaller value for $ZnFe_2O_4$–Ag (0.008 emu/g) than for $ZnFe_2O_4$ (0.054 emu/g) or Fe_3O_4 (0.055 emu/g). The magnetic behaviors are related to the nonequilibrium distribution of Fe^{3+} in the spinel A and B sites, causing significant crystal defects. Thus, a lower coercivity (Hc) for $ZnFe_2O_4$ (0.14 kOe) and $ZnFe_2O_4$–Ag (2.5%) (0.13 kOe) has resulted as compared to that for Fe_3O_4 (0.21 kOe). The cationic distribution between tetrahedral and octahedral sites can increase the cation inversion parameter, improving the magnetization; mostly, it depends on the manner in which the Fe^{3+} is being distributed in the geometries.[30] A decrease in the surface anisotropy is attributed to the deposition of Ag NPs.

Diffusion Reflectance Spectra (DRS). For all the samples, the DRS (Figure S3) was recorded, observing a broad-band around 298 nm. The peak intensity was diminished for $ZnFe_2O_4$–Ag NPs at 300 nm as compared to other samples. Moreover, if the deposition amount of Ag NPs on $ZnFe_2O_4$ is increased, the Ag NPs become nonplasmonic (>0.75 atom %). The bandgap energy was determined by using the DRS. (i) Tauc method: $\alpha = A(h\nu - E_g)^2/\lambda$ for direct (allowed) and $\alpha = A(h\nu - E_g)^{1/2}/\lambda$ for indirect (allowed) (α = absorption coefficient; A = absorption constant for indirect transitions depending on the transition probability). The extrapolation of the horizontal y-axis[31] against the x-axis (photon energy, $h\nu$) intercepts the bandgap energy. (ii) In the Kubelka–Munk function $F(R)$,[32] the diffuse absorption spectra were converted into the reflectance spectra through which the band gap energy was calculated as indicated in eqs S3 and S4.[33] In the present work, the Tauc's plot was obtained by extrapolating $(\alpha h\nu)^{1/2}$ against the photon energy, calculating the indirect bandgap energy as 2.00 eV for Fe_3O_4, 1.9 eV for $ZnFe_2O_3$, and 1.76 for $ZnFe_2O_4$–Ag. The results show a decrease in the bandgap energy for $ZnFe_2O_4$–Ag, which assists the hot electron injection from Ag NPs to the CBs; consequently, it increases the half-life of photoinduced electrons as described in Scheme 1.[34] This is consistent with DFT-DOS spectra, where the Fermi energy level of Ag NPs has been positioned just below the conduction band (CB), producing a Schottky barrier in the interface of $ZnFe_2O_4$. It is known that ligand metal charge transfer (LMCT) is accounted for the color of iron oxide (Fe_3O_4, Fe^{3+}, $3d^5$) because of the forbidding electronic transitions (both spin and d–d transitions). Yet, if the magnetic coupling has occurred appropriately between next-nearest-neighbor Fe^{3+} ions, then these d–d transitions ($^6A_1 \rightarrow {}^4T_1$, $^6A_1 \rightarrow {}^4T_2$, and $^6A_1 \rightarrow {}^4E$) are allowed as it depends upon the Fe-to-Fe distance. The quantum yields (Φ) were determined by measuring the transmitted energy (γ) at 400 nm as reported[35] as 0.60 for $ZnFe_2O_4$, 0.25 for $ZnFe_2O_4$–Ag (1.0%), 0.70 $ZnFe_2O_4$–Ag (1.5%), 0.66 for $ZnFe_2O_4$–Ag (2.0%), and 0.66 for $ZnFe_2O_4$–Ag (2.5%), showing that the disposition of Ag NPs (1.5–2.5%) gives a good quantum yield of $\Phi > 0.60$.

Adsorption Studies. The adsorption behavior of RhB over $ZnFe_2O_4$–Ag NPs (2.5%) was studied (Figure 5a) by measuring its concentration at 553 nm, and then plotted against the time to obtain an equilibrium constant (q_e). The adsorption data were analyzed by fitting in the following models in Langmuir (red), Freundlich (green), and Redlich–Peterson (blue) equations.[36] The results show that the Freundlich and Redlich-Peterson models allowed a good fit as compared to the Langmuir model for $ZnFe_2O_4$–Ag (2.5%) and Fe_3O_4. The maximum adsorption constant results in q_m = 206 mol/g for $ZnFe_2O_4$–Ag (2.5%), rather than for $ZnFe_2O_4$ (2.36×10^{-3} mol/g) or for Fe_3O_4 (2.43 mol/g), respectively. Notably, $ZnFe_2O_4$–Ag NPs follow the Redlich-Peterson model, resembling Langmuir adsorption at low concentrations, but $ZnFe_2O_4$, yielded a poor plot (see Figure S4).

Photocatalytic Degradation of RhB. The photocatalytic properties of $ZnFe_2O_4$Ag (2.5%), $ZnFe_2O_4$, and Fe_3O_4 were analyzed under UV or visible lights using RhB as a model pollutant. The substrate concentration was measured through

https://doi.org/10.1021/acsomega.2c03153
ACS Omega 2022, 7, 33985–34001

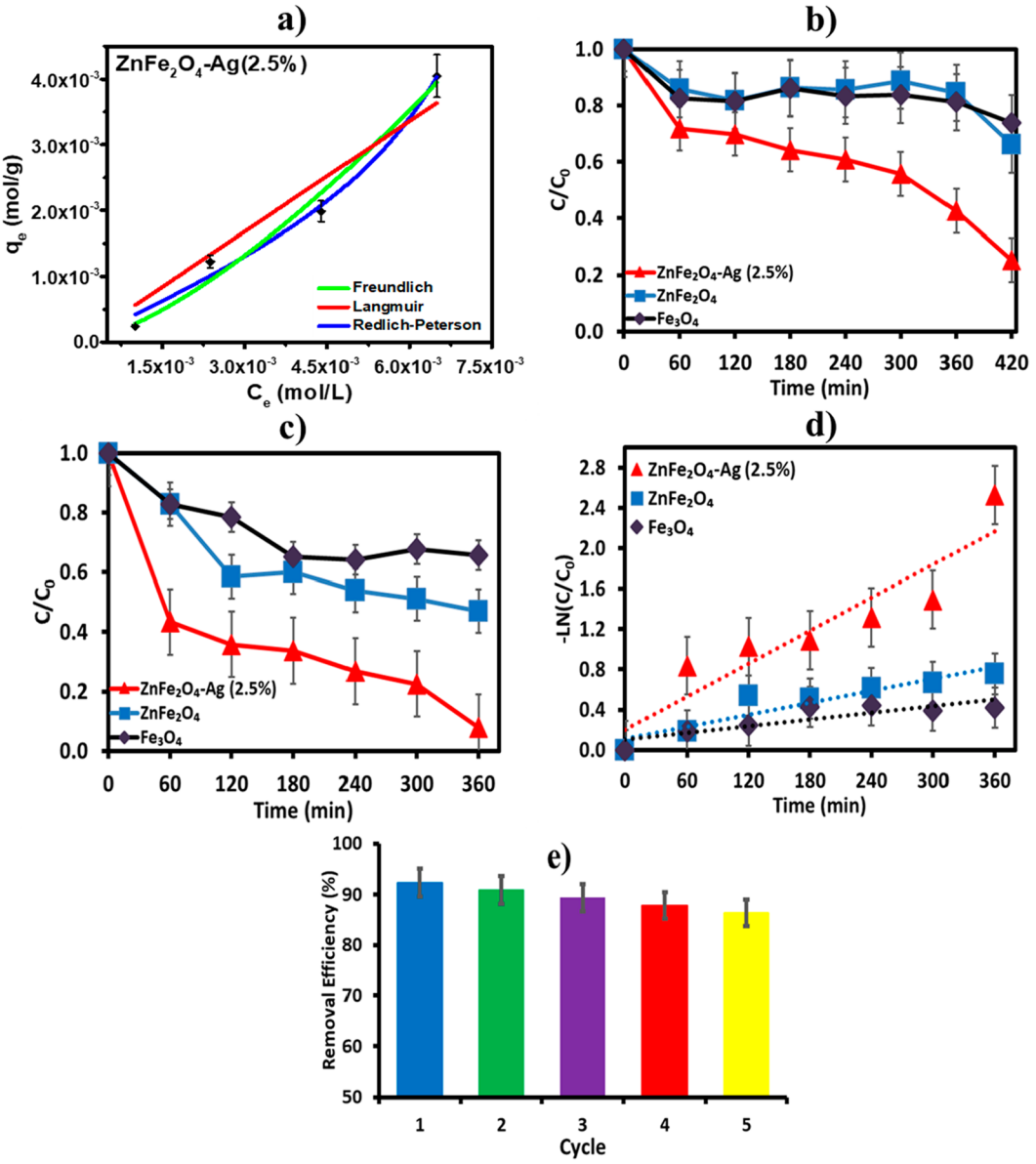

Figure 5. (a) RhB adsorption: Nonlinear fit for Redlich-Peterson, Freundlich, and Langmuir, isotherms for $ZnFe_2O_4$–Ag (2.5%). (b) Plot of (C/C_0) vs time under UV light; (c) Plot of (C/C_0) vs time under visible light. (d) Plot of ($-\ln C/C_0$) vs time under visible light; (e) Evaluation of stability and reusability of $ZnFe_2O_4$–Ag (2.5%).

absorbance intensity at 553 nm and plotted against the time (Figure 5b,c). A considerable change of color (pink to colorless) was observed, and it was reflected in the absorption maximum by shifting λ_0 = 553 to λ_f = 538 nm during the oxidation (Figure S4a,b). The degradation follows a first-order kinetics, and the rate constant (k) was calculated using the equation $\ln[C] = -kt + \ln[C_0]$ (Figure 5d). The results reveal a greater value for $ZnFe_2O_4$–Ag (2.5%) ($k = 2.6 \times 10^{-3}$ min^{-1}) than for $ZnFe_2O_4$ ($k = 5.0 \times 10^{-4}$ min^{-1}) or for Fe_3O_4 ($k = 4.1 \times 10^{-4}$ min^{-1}) under UV light. The oxidation of RhB was about 74.5% for $ZnFe_2O_4$–Ag (2.5%), 34.2.3% for $ZnFe_2O_4$, and 27.2% for Fe_3O_4 under UV light. While it was 92.2% for $ZnFe_2O_4$–Ag (2.5%), 52.4% for $ZnFe_2O_4$, and 40.8% for Fe_3O_4 under visible light observing a greater oxidation rate for $ZnFe_2O_4$–Ag (2.5%) ($k = 5.5 \times 10^{-3}$ min^{-1}) as opposed to others ($k = 2.0 \times 10^{-3}$ min^{-1} for $ZnFe_2O_4$ and k = 1.1×10^{-3} min^{-1} for Fe_3O_4). The present results are consistent with the reported work, that is, for bare $ZnFe_2O_4$ and Bi_2WO_6, the RhB photodegradation was just 28% and 44% under visible light, respectively; however, the percentage was increased to 76% when it was modified to $Bi_2WO_6/ZnFe_2O_4$.[37] For $ZnFe_2O_4$, it was reported around 60%,[38] and the value was relatively higher in the other studies.[39,40] This indicates that without any catalyst, the oxidation of RhB was found to be less than 5.0% even after 3 h of irradiation, and it was increased to 31% after 3 h of irradiation in the presence of $ZnFe_2O_4$ ($Zn_xFe_2O_4$). Nonetheless, a significant increase in degradation (93%) was reported if the $Zn_xFe_2O_4$ was decorated with Au.[41] It is known that the photocatalytic activity of pure $ZnFe_2O_4$ is relatively poor because of the rapid recombination effect[40,42] which was reduced considerably for $ZnO/ZnFe_2O_4$ or Ag-$ZnFe_2O_4$@rGO composites.[39,43] The removal of RhB was about 90% in the present work, and some studies have reported more than 90%; this is probably due to the experimental conditions adopted for the oxidation, including the concentration of H_2O_2[44,45] and the magnetization

https://doi.org/10.1021/acsomega.2c03153
ACS Omega 2022, 7, 33985−34001

Table 3. Different Ferrite and Nonferrite Materials as Photocatalysts for the RhB

Nanomaterial	Size (nm)	Reaction time (min)	Light source	Removal (%)	ref
TiO_2/GO nanocomposites[a]	50	20	UV	90.56	49
Fe_3O_4/ZnO/GO[b]	5.0	50	UV	100	50
MWCNT−$CuNiFe_2O_4$[b]	3−14	30	UV	100	51
MWCNTs/$CoFe_2O_4$[b]	32	60	UV	95.2	52
$ZnFe_2O_4$@g-C_3N_4	5.0	30	Visible	96.2	53
$ZnFe_2O_4$	20	300	Visible	100	54
ZnS−$ZnFe_2O_4$	20	90	UV	97.7	55
$Ni_xZn_yFe_2O_4$	30	180	Sunlight	94.0	56
$Co_{0.7}Zn_{0.3}Fe_2O_4$	20	40	Sunlight	∼20.0	57
$ZnFe_2O_4$	19	30	Visible	60.0	38
$ZnFe_2O_4$	12	60	Sunlight	94.0	58
$ZnFe_2O_4$/TiO_2/flake graphite	100−1000	30	UV	99.0	59
ZnO	500−400	180	Solar	100	60
TiO_2/C	20−50	4	Visible	100	61
TiO_2 P-25	20	30	UV	55.0	62
CQD/ZnO	10−30	120	UV	80.0	63
CQD/Cu/N/Ag_3PO_4	200−300	60	LED	95.5	64
Ag_3PO_4/SAPO-34 (SAPO-34= silicon aluminum phosphate)	100−200	30	Visible	90.8	44
CQD/CdS	10−50	180	Visible	90.0	65
$Cu_{2-x}Se$/CdS	-	180	Visible	∼95	45
CQDs/Bi_2MoO_6	20	120	Visible	100	66
CQDs/BiOCl/BiOBr	40	60	Visible	100	67
Sr/Ce/AC	50	120	Solar	91.0	68
ZnO/Au	30	180	UV	95.0	69
$ZnFe_2O_4$Ag (2.5%)	20 nm	420	UV	74.5	Present work
$ZnFe_2O_4$,	10−15	420	UV	34.2	Present work
Fe_3O_4	10−15	420	UV	27.2	Present work
$ZnFe_2O_4$Ag (2.5%)	20	360	Visible	92.4	Present work
$ZnFe_2O_4$	10−15	360	Visible	52.3	Present work
Fe_3O_4	10−15	360	Visible	46.3	Present work

[a]Degradation of acid orange 7 dye. [b]Degradation of acid blue 113 dye.

associated agglomeration. Thus, $ZnFe_2O_4$−Ag (2.5%) is shown as an effective photocatalyst because the plasmonic metal deposition on $ZnFe_2O_4$ promotes favorable active sites, supporting the photoactivation process. In the literature, the removal of pollutants by $ZnFe_2O_4$-based composites was reported.[39,40] The reusability and stability of $ZnFe_2O_4$−Ag (2.5%) was recovered magnetically and reused up to five times for the degradation of RhB. The results (Figure 5e) show an excellent performance in reusability with high efficacy during the recycles, and the composite was considerably stable even after five consecutive cycles.

Since the RhB can act as a photosensitizer altering the efficiency of the oxidation, we have also used phenol as a colorless pollutant to assess the catalytic degradation efficiency. The phenol oxidation was about 64.5% in the presence of $ZnFe_2O_4$−Ag as compared to 39.4% for $ZnFe_2O_4$ and 28.5% for Fe_3O_4 under visible light (Figures S5a and S6c). So, if $ZnFe_2O_4$ and $ZnFe_2O_4$−Ag NPs are excited by photons under visible light, it generates electron−hole pairs; consequently, the photogenerated electrons can be transferred from the CB of $ZnFe_2O_4$ (−1.54 V vs NHE)[43] to the surface of Ag NPs ($E_{Ag+/Ag}$, 0.80 V vs NHE) since Ag NPs can absorb visible light because of the SPR effect. The plasmon-induced electrons of Ag NPs can also flow easily to CB of $ZnFe_2O_4$; as a result, the charge separation can be enhanced. Moreover, a portion of the CB electrons of $ZnFe_2O_4$ can be shifted toward the Ag^+ ions, reducing some Ag^+ ions to Ag NPs. However, other electrons would be scavenged by O_2 molecules in water to produce superoxide free radicals ($*O^{2-}$, reactive active species). Additionally, the reactive holes in VB could oxidize the pollutants efficiently due to the more negative potential of the VB ($ZnFe_2O_4$, 0.38 V vs NHE)[43,46] relative to that of H_2O (E_{OH/H_2O} = 2.87 V vs NHE).[43,47] The EPR measurements (Scheme 1b) were carried out in a quartz tube at room temperature in aqueous suspensions using a Jeol JES-TE300 spectrometer operating in X-Band fashions at 100 kHz modulation frequency. The external calibration of the magnetic field was performed using a Jeol ES-FC5 precision gaussmeter with a 5350B HP microwave frequency counter. Spectral acquisition and manipulations were performed using ES-IPRITS-TE software. EPR spectra recorded show that there are formation radicals that are oxidizing the substrate. The mismatching of the heterostructure of $ZnFe_2O_4$ (cationic valence and coordination number, Zn^{2+} for tetrahedral, Fe^{3+} for octahedral in Zn−O−Fe) induces the polarizing capacity of Fe^{3+} over Zn^{2+} contributing more surface charge on $ZnFe_2O_4$−Ag. The DFT-E_g determined shows that the value is lower for $ZnFe_2O_4$/Ag when compared to that for $ZnFe_2O_4$ (see computational section). Previous reports[48] establish the formation of prominent intermediates for the oxidation of RhB, and the oxidation of RhB by different ferrite and nonferrite materials is summarized in Table 3.

This is consistent with the DFT studies, where the total energy of the intermediates shows a feasible cleavage of the diphenyl group by OH radicals (Scheme 2).

https://doi.org/10.1021/acsomega.2c03153
ACS Omega 2022, 7, 33985−34001

Scheme 2[a]

a)

b)

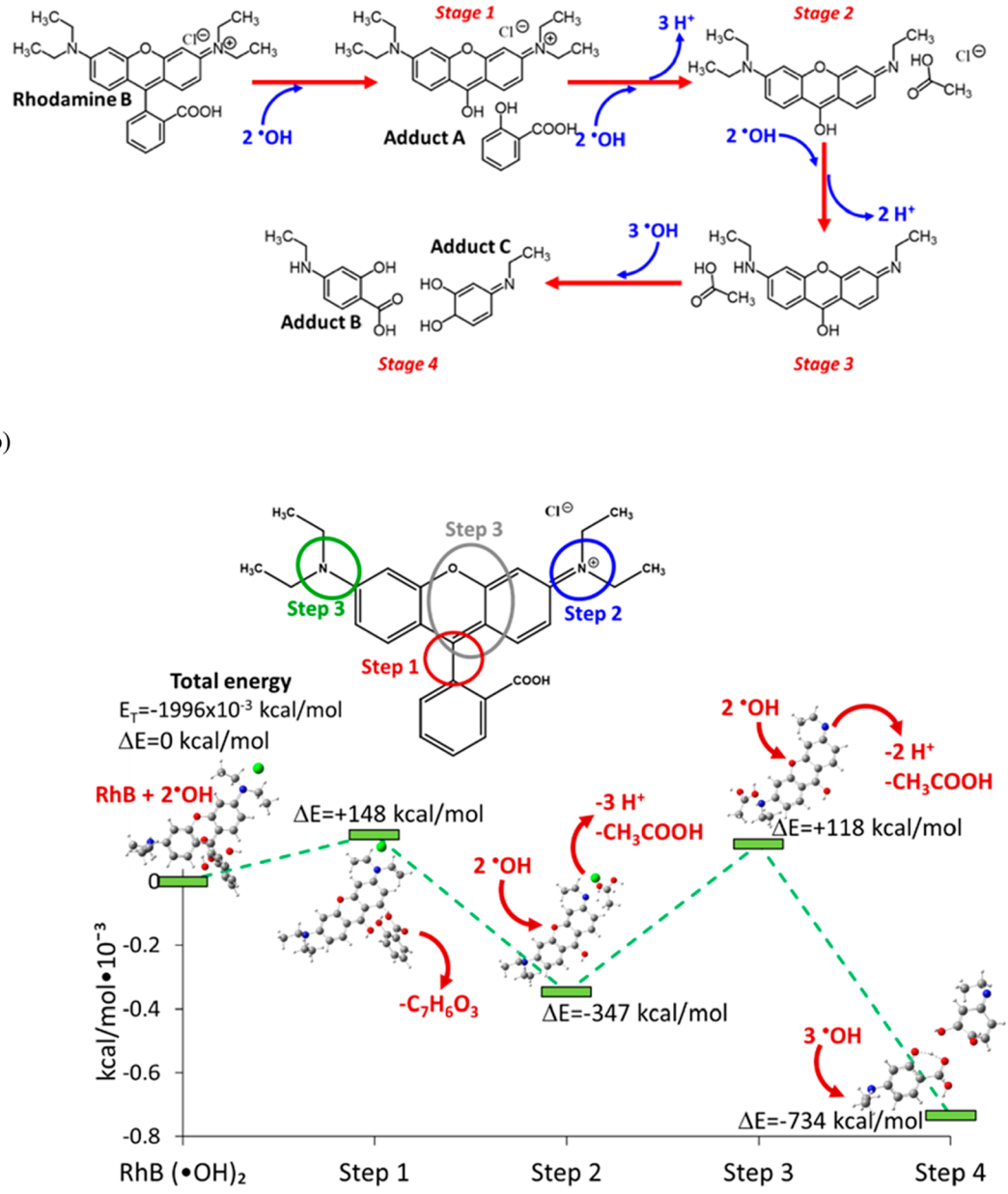

[a](a) Illustration of RhB oxidation; (b) total energy of intermediates modeled by DFT at 6-311G/BB95K.

$$ZnFe_2O_4 - Ag + h\nu \rightarrow ZnFe_2O_4 - Ag(h^+_{vb} + e^-_{cb}) \quad (1)$$

$$h^+_{vb} + H_2O \rightarrow H^+ + \cdot OH \quad (2)$$

$$h^+_{vb} + OH^- \rightarrow \cdot OH \quad (3)$$

$$O_2^- + e^-_{cb} \rightarrow O_2\cdot^- \quad (4)$$

$$O_2\cdot^- + e^-_{cb} + 2H^+ \rightarrow H_2O_2 \quad (5)$$

$$O_2\cdot^- + H_2O_2 \rightarrow \cdot OH + OH^- + O_2 \quad (6)$$

$$e^-c_b + H_2O_2 \rightarrow \cdot OH + OH^- \quad (7)$$

$$2\cdot OH \rightarrow H_2O_2 \quad (8)$$

Point of zero charge (PZC) was determined by applying the pH drift method for $ZnFe_2O_4$ and $ZnFe_2O_4$–Ag (2.5%). The results (see Figure S7) show 7.9 for $ZnFe_2O_4$. For the addition of Ag on $ZnFe_2O_4$, the PZC value gradually decreases to 7.15 for $ZnFe_2O_4$–Ag (2.0) and 7.6 for $ZnFe_2O_4$–Ag (1.0). A higher rate constant results at low pH in contrast to the high pHs since the production of OH radicals is more feasible at low pH than at high pH where the presence of OH^- ions is prominent.

Density Functional Theory (DFT). We explained the oxidation of RhB through the DFT studies.[70] The structure of intermediates was optimized, and the total energy with respect to the RhB+2•OH system was determined (see Scheme 2).

https://doi.org/10.1021/acsomega.2c03153
ACS Omega 2022, 7, 33985−34001

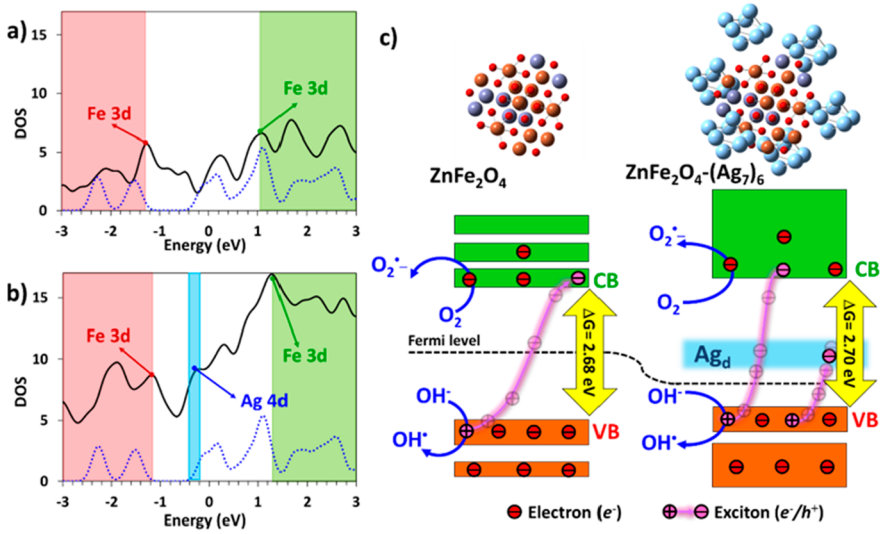

Figure 6. DOS for (a) bare $ZnFe_2O_4$ and (b) $ZnFe_2O_4$−$(Ag_7)_6$ denoting valence bands (red area), conduction bands (green area), and Ag_{4d} states; DOS of Ag_7 is presented as a blue dashed line. (c) Proposed band energy for $ZnFe_2O_4$ and $ZnFe_2O_4$−$(Ag_7)_6$ based on jellium exciton approach.

The photo-oxidation occurred through the attack of two OH radicals that cleaved the benzoic group (RhB structure), as it required about +148 kcal/mol to form the first adduct (Step 1, nonspontaneous process). In step 2, the OH radical is attacked at the tertiary imine undergoing easy oxidation to produce ethanoic acid because of low total energy (−347 kcal/mol). In step 3, $^{\bullet}$OH radicals attack at the tertiary amine attached to the aromatic center, yielding acetic acid as an endothermic process (+118 net kcal/mol) with respect to the starting system; yet, it is more feasible than the first step. The last step is highly exothermic (−734 kcal/mol) and it involves the formation of two products (xanthene core to splitting) by taking three OH radicals.

Computational Modeling of $ZnFe_2O_4$−Ag. The structural and electronic properties of $ZnFe_2O_4$−Ag are analyzed, and the energy level of the valence (VB) and conduction (CB) bands are determined. DFT structural optimization of $ZnFe_2O_4$−Ag was also performed using periodic functional HSEh1PBE with the LANL2DZ basis set. First, the structure of $ZnFe_2O_4$ was constructed after considering its spinel *fcc* geometry consisting of 56 atoms (8 Zn, 16 Fe, and 32 O). The total volume resulting was 567.93 Å^3 (a = 8.281 Å, b = 8.20 Å, and c = 8.283 Å). Similarly, the structure of the Ag_7 cluster was also optimized to attach to the surface of $ZnFe_2O_4$ yielding $ZnFe_2O_4$−$(Ag_7)_n$ (Figures S8, S9, and S10). After analyzing the electronic properties, it was noticed that CB was formed by mixing empty d orbitals from both Zn^{2+} and Fe^{2+} ($ZnFe_2O_4$); while for VB, only empty d orbitals from Fe^{3+} were involved. Apparently, oxygen 3p orbitals have not contributed significantly to the formation of either CB or CV band. The overall electron density of unoccupied states was increased if the Ag atoms adhered to $ZnFe_2O_4$ due to the participation of 4d orbitals in CB (Ag cluster). As a result, new sets of electronic states, holding either e^- or h^+, are formed; the formation of charged pairs has been seen through the excitons, reducing the recombination effect, and it has enhanced the photon harvesting capability. This is consistent with ZnO, Fe_3O_4, TiO_2, and ZnS systems.[71]

The metallic bonds present in $ZnFe_2O_4$ are involved in the delocalization associated with the Ag clusters as stated in the jellium model[72] and the resulting electronic shell has resembled that in other studies.[73] The total energy (E_t) of the systems was defined by the interaction of $ZnFe_2O_4$ (E_{zf}) with a number (n) of $(Ag_7)_n$ clusters (eq 9):

$$E_t = E_{zf} + (E_{Ag} \cdot n) \tag{9}$$

The interface between Ag5 d and Fe^{2+} 3 d influences the degree of interaction in the electronic states. If the energy difference is yielded as $\Delta E \geq 0$, then the Ag cluster has interacted preferably on the $ZnFe_2O_4$ system, producing a synergistic effect. On the other hand, if the energy difference is $\Delta E \leq 0$, it would not generate an energetically positive impact on the interaction of the Ag clusters with $ZnFe_2O_4$. For $ZnFe_2O_4$−$(Ag_7)_n$ (n = 1,2), a high stability results, increasing the electron density at the edge of occupied states (VB), and the same notation was observed in the edge of unfilled states (CB). As a result, the contribution of electron density from Ag4 d to the bandgap energy is significantly reduced to 1.11 for $ZnFe_2O_4$−$(Ag_7)_1$ and to 1.02 eV for $ZnFe_2O_4$−$(Ag_7)_2$ (Figure S11). In contrast, for $ZnFe_2O_4$−$(Ag_7)_3$ and $ZnFe_2O_4$−$(Ag_7)_4$, an unstable geometry was obtained, as Ag d states are located at the band edges, increasing the band gap energy.

For the deposition of Ag on $ZnFe_2O_4$ such as $ZnFe_2O_4$−$(Ag_7)_n$ (n = 5,6), a decrease in total energy was seen. If the size of the cluster is augmented, the net bandgap energy is 2.55 for $(Ag_7)_5$ and 2.46 eV for $(Ag_7)_6$ (Figure S8). Notably, the calculated bandgap energy is usually greater as compared to the experimental values due to the quantization of states present in small-scale systems.[74] For $ZnFe_2O_4$, the experimental bandgap energy (1.9 eV)[75] is relatively smaller than the calculation values (2.7−3.0 eV) owing to the quantization of orbitals. If the Ag_7 cluster was placed on $ZnFe_2O_4$, a new set of unoccupied energy states has been generated by lying between CB and VB right above the Fermi level (energy state of Ag d, $E \approx -0.4 \pm 0.1$ eV). It forms an e^-/h^+ pair excitons occurring between VB and Ag d, which facilitates the "hot electron injection" into CB by increasing the electron density (Figure 6c). The filled shells contribute considerably to the stability of $ZnFe_2O_4$−Ag. However, a specific ratio of $ZnFe_2O_4$:Ag can enhance the photocatalytic properties, particularly, the amount of Ag NPs deposition (i.e., a certain percentage) allows the surface modification for $ZnFe_2O_4$.[76]

https://doi.org/10.1021/acsomega.2c03153
ACS Omega 2022, 7, 33985−34001

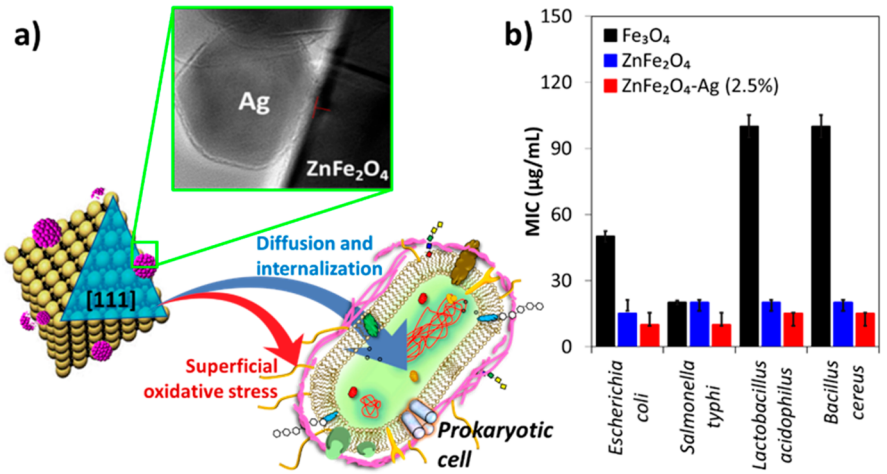

Figure 7. Bacterial inhibition: (a) proposed mechanism of action; (b) MIC data of antibacterial studies.

Yet, a marginal contribution from the Ag cluster was detected in the full DOS spectra (Figure 6a,b).

Antibacterial Studies. The antibacterial properties of $ZnFe_2O_4$–Ag (2.5%), $ZnFe_2O_4$, and Fe_3O_4 were also studied against different pathogens (*Staphylococcus aureus, Bacillus cereus, Escherichia coli*, and *Salmonella typhi*) (Figure 7). The results show a significant bacterial growth inhibition in the presence of both $ZnFe_2O_4$ and $ZnFe_2O_4$–Ag NPs (Table S5). The existence of Ag atoms on $ZnFe_2O_4$ ($ZnFe_2O_4$–Ag NPs) enhances further antimicrobial activities, resulting in the lowest MIC value for *B. cereus* as 62.22 µg/mL for $ZnFe_2O_4$–Ag NPs, ~82.96 µg/mL for $ZnFe_2O_4$, and ~414.82 µg/mL for Fe_3O_4 NPs. The same behavior was observed for other pathogens (Table 4, Figure 6b) due to Ag^+ or Ag NPs which react with an organic functional group (thioglucoside, carboxyl, hydroxyl), inhibiting the bacterial growth through altering the cellular functions. Thus, the entrance of NPs into the bacterial cell affects the electron transfer system in the enzyme/protein gene expression.[77]

Table 4. Antibacterial Data of Zinc Ferrites

	Minimal inhibitory concentration [uM]			
	Gram-Positive		Gram-negative	
Inhibitor	*Bacillus cereus*	*Lactobacillus acidophilus*	*Escherichia coli*	*Salmonella typhi*
$ZnFe_2O_4$	82.96	82.96	62.22	82.96
Fe_3O_4	414.82	414.82	207.41	82.96
$ZnFe_2O_4$–Ag	62.22	62.22	41.48	41.48

It is still unclear how a specific pathway is being adopted for the bacterial inhibition; however, the release of Ag^+ from $ZnFe_2O_4$–Ag NPs is expected, and it generates ROS (H_2O_2, $^1O_2$, and $OH^•$) which can interact with cells to inhibit the DNA replication.[78] The generation of radicals from the sample was proven by the EPR studies at room temperature in aqueous suspensions (see Scheme 1b), showing that there is a formation of free radicals, consisting of the reported studies.[79] It is also coherent with other reports that ZnO NPs can produce a variety of ROS (H_2O_2, $^•OH$, and $^1O_2$) in aqueous solution, and it was also further proven by the EPR technique.[80] So, ZnO in Fe_2O_3 plays a decisive role in the generation of ionic signals between cells and intercellular cytoplasmic organoids.[81] The external oxidative species can be easily diffused into a single-layer cell membrane (Gram-Positive: *Lactobacillus acidophilus* (*Bacillus cereus*) as compared to a three-layer membrane configuration of *E. coli and S. Typhi* (Gram-negative type). Small size particles can improve the particle–cell contacts to enhance the intrinsic toxicity, and it suggests that the size of $ZnFe_2O_4$ and $ZnFe_2O_4$–Ag NPs (<50 nm) encourages the inhibition of cell growth. We have also studied the behavior of *S. cerevisiae* cells with $ZnFe_2O_4$–Ag (2.5%) in confocal fluorescence microscopy, showing the increasing diffusion of $ZnFe_2O_4$–Ag NPs (2.5%) into the cell as it emits blue light at 405 nm.

EXPERIMENTAL SECTIONS

Chemical, Materials, And Characterization Details. $Zn(CH_3COO)_2$, $AgNO_3$, $NaBH_4$, Na_2CO_3, MeOH, CH_3CN, and polyethylene glycol (Sigma-Aldrich) were used as received. For the inoculation, cysteine Tryptic Agar (CTA, BIOXON), Mueller Hinton Agar (MHA), and Nutritive Broth (DIBICO) were employed. For cell culture, Petri dishes (90 × 15 mm) and 96-wells plates were considered.

Fe_3O_4 NPs. KOH (1.0 M, 3.57 g, 50 mL) dissolved in water was added to an aqueous solution of $FeCl_2$ (15 mM, 50 mL), and the resulting mixture was stirred for 25 min before it was transferred to a Teflon (100 mL) autoclave, which was then heated at 180 °C for 18 h. After the mixture slowly cooled, a dark-colored product was obtained which was washed with ethanol three times, followed by cold acetone. Finally, after deionized water was used to remove excess KOH, the product was treated thermally in a furnace at 75 °C overnight. Yield: 23.5%.

$ZnFe_2O_4$ NPs. As reported previously,[82] $FeSO_4·7H_2O$ (1.0 g, 3.59 mmol) and $Zn(OAc)_2·2H_2O$ (0.43 g, 1.95 mmol) were dissolved in an aqueous solution (40 mL) containing $N_2H_4·H_2O$ (10 M, 0.05 mmol). The resulting mixture was transferred to a Teflon-contained autoclave for heating for 14 h at 180 °C. A brownish sample was obtained after the mixture was centrifuged (6000 rpm for 15 min), and it was washed with different ethanol/water mixtures (25:75; 50:50), followed by pure EtOH). The product was dried in an oven at 60 °C for 13 h, yielding 19.1% (Scheme 3).

Ag Doping of Fe_3O_4 and $ZnFe_2O_4$ NPs. Using the modified procedure,[83] a nanocomposite was prepared. Briefly,

https://doi.org/10.1021/acsomega.2c03153
ACS Omega 2022, 7, 33985−34001

Scheme 3. Preparation of Zinc Ferrite

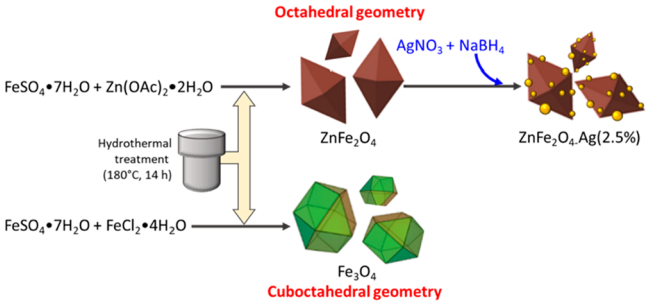

$ZnFe_2O_4$ NPs (40 mg) were suspended in 50 mL of ethanol, and the mixture was stirred at 4 °C under dark conditions. To this suspension, $AgNO_3$ solution (2.36 mL, 2.0 mM) was slowly added under stirring, and then $NaBH_4$ solution (3.1 mL, 10 mM) was added. After the reaction, the sample was separated magnetically and dried at 60 °C for 12 h. Yield: ca. 35 mg (47.29% Fe and 21.41% Zn). The same procedure was adopted for the deposition of Ag at different proportions (1.18 mL, 1.0%; 1.77 mL, 1.5%; 2.36 mL, 2%; 2.95 mL, 2.5%).

Adsorption Studies. The adsorption behavior of $ZnFe_2O_4$–Ag (2.5%), $ZnFe_2O_4$, and Fe_3O_4 with RhB dye was analyzed. Typically, the adsorbent (10.0 mg) was added to the RhB solution (10 mL, 1.0×10^{-6} M to 7.5×10^{-6} M) in an amber bottle, stirred for 15 h in the dark room, and then centrifuged at 15 000 rpm for 10 min to collect the supernatant. The equilibrium concentration of RhB was calculated by measuring the absorbance at $\lambda_{max,\ RhB}$ = 554 nm, and corroborated with the standard plot. The equilibrium capacity of adsorption q_e (mol/g) was determined by employing the equation $q_e = (C_0 - C_e)$ V/m, where C_0 (mol/L) = [RhB] at time 0; C_e = [RhB] at equilibrium time, V (mL) = volume of the dye solution, and m (mg) = adsorbent mass.

Photocatalytic Studies. Photocatalytic degradation of RhB dye was studied using $ZnFe_2O_4$–Ag (2.5%), $ZnFe_2O_4$, and Fe_3O_4 under UV or visible light. The reactor was equipped with a xenon lamp (UV irradiation, Newport 361, 1000 W) having a Pyrex glass filter (λ = 390 nm). The catalytic sample (15 mg) was mixed with RhB (20 mL, 2.0 μM) and allowed to degrade under the photoreactor. The concentration of RhB was determined at different time intervals (60, 120, 180, 240, and 300 min) at λ_{max}, RhB. Similarly, the degradation of an aqueous solution of RhB (5.0 mL, 10 μM) with the sample (Fe_3O_4, $ZnFe_2O_4$, or $ZnFe_2O_4$–Ag (2.5%, 0.2 mg/mL) was observed under visible light (halogen lamp, 1.0 m, 239 W/m^2). Hydrogen peroxide (0.3%) was used for the activation. Separately, the photocatalytic oxidation of phenol (5 mL, 100 μM) was studied under visible light (halogen lamp, 1.0 m, 239 W/m^2) in the presence of Fe_3O_4, $ZnFe_2O_4$, or $ZnFe_2O_4$–Ag (2.5%, 0.2 mg/mL). The concentration of phenol was determined through the 4-amino antipyrine method. Phenol solution (1.0 mL) was first mixed with NH_4OH (0.5 N, 25 μL) to adjust the pH of the solution (7.9 ± 0.1), and then to which 4-aminoantipyrine (10 μL) was added, followed by $K_3[Fe(CN)_6]$ (10 μL). The resulting solution was stirred for 15.0 min in the phosphate buffer. The solution turned red, facilitating the measurement of the substrate concentration in the visible region in the spectrophotometer.

Antibacterial Activity. Antibacterial properties of the samples $ZnFe_2O_4$–Ag (2.5%), $ZnFe_2O_4$, and Fe_3O_4 were studied using different bacterial strains (two strains of Gram-positive (*Staphylococcus aureus* and *Bacillus cereus*) and two of Gram-negative strains (*Escherichia coli* and *Salmonella typhi*), which were obtained from WFCC/WDCM-100, Faculty of Chemistry, UNAM, Mexico, and maintained in Cysteine Tryptic Agar (CTA, 4 °C). The characterization of strains was followed as indicated in ref 84. (see Supporting Information).

Minimal inhibitory concentration (MIC) was determined against bacteria as reported previously.[83] The strain standardization was performed in the suspension of Mueller-Hinton nutritive agar to reach 1.0×10^6 CFU mL^{-1}. A solution of Fe_3O_4, $ZnFe_2O_4$, or $ZnFe_2O_4$–Ag was first prepared as a stock dilution and then diluted from 5 to 200 μg·mL^{-1}.

Bacterial qualitative assays were evaluated with the assistance of the disk diffusion method as described elsewhere.[84,85,26,86] Mueller Hinton Agar plates were first inoculated with previously standardized inoculum, then the sterile paper discs (Whatman No.1, 6.0 mm in diameter) were placed on the surface of the plates. After the solution of Fe_3O_4, $ZnFe_2O_4$, or $ZnFe_2O_4$–Ag NPs (20 μL, 30.0 mM) were dispersed on the surface of each disc, the plates were then incubated for 24 h at 35 °C under visible light. During the measurement of diameters (mm) of cell growth inhibition zones, an aqueous solution of *p*-iodonitrotetrazolium chloride (10 μL, 10 mM) was added as an indicator.

Computational Procedure. The structural optimization of $ZnFe_2O_4$ and $ZnFe_2O_4$–Ag atoms was performed by Density Functional Theory (DFT) using a periodic functional like the HSEh1PBE LANL2DZ basis set. Single crystal structural data of $ZnFe_2O_4$ were obtained from the Chem Tube 3D database, University of Liverpool, for optimization. The model consists of a spinel *fcc* cubic structure (56 atoms: 8 Zn, 16 Fe, and 32 O), and a = 8.281 Å, b = 8.20 Å, and c = 8.283 Å to result to a total volume of 567.93 Å^3. Silver clusters $(Ag_7)_n$ (n = 1–7) were placed over $ZnFe_2O_4$ and optimized the cell structure. The clusters were distributed evenly on each of the crystal unit facets (Figure S7). To determine the electronic structure, ultrasoft pseudopotentials (USP) were used, and for the solvent effect, an IEF-PCM was employed.

Physical Measurements. X-ray diffraction (XRD) analysis was carried out by using a diffractometer (Rigaku RU300) with Cu Kα radiation (λ = 1.5406 nm) at 2θ between 20° and 80°. The obtained XRD data for the samples were compared to those reported in the crystallographic data index No. 0002576F AMCSD (American Mineralogist Crystal Structure Database). The observed crystalline structure for $ZnFe_2O_4$ and $ZnFe_2O_4$–Ag corresponds to *fcc*, for normal spinel (*fd3m*) where Zn^{2+} occupies the octahedral and tetrahedral geometries while Fe^{2+} is seated at the tetrahedral site. The crystal size was calculated using the following equations

$$\text{crystallite size } (\tau) = \frac{0.9\lambda}{\beta \cos\theta} \text{ where } \beta = \sqrt{\beta_{obs}^2 - \beta_0^2} \tag{10}$$

β_{obs} = fwhm of refection; β_0 = instrumental fwhm minimum; λ = wavelength

$$\tau = \frac{0.9\lambda}{\beta \cos\theta} \tag{11}$$

where τ = mean size of the crystal lattice; λ = X-ray wavelength; β = fwhm in radians, and θ = Bragg angle. Lattice constant a can be calculated from the Miller indices (h, k, l) using the relation of $a = d(h^2 + k^2 + l^2)^{1/2}$, where d (interplanar

https://doi.org/10.1021/acsomega.2c03153
ACS Omega 2022, 7, 33985−34001

spacing) is calculated by using the Bragg law. Crystalline parameters: $a = b = c = 8.3515$ Å (a 25 °C) agree with the cubic phase. FT-IR spectrum (model 100/100N FT-IR, PerkinElmer) and a UV−vis spectrophotometer (PerkinElmer 25, range of 190 to 1100 nm) were used to record the vibrational and optical absorption spectra of the samples, respectively. The scanning electron microscope (JEOL JSM-5600LV) is equipped with an energy dispersive X-ray spectrometer (EDS microanalyzer) to obtain the SEM images. The samples were prepared by placing a drop of the NPs solution on a 300 mesh copper grid and collecting the data in 15 different spots. The size and nature of crystalline NPs were studied by a transmission electron microscope (TEM, JEOL 2010) with an accelerating voltage of 100 kV and high-resolution transmission electron microscopy in a JEOL 2010 FE-TEM. An X-ray photoelectron spectroscope (XPS, K Alpha Thermo-Fisher Scientific Instruments), where the chamber pressure was 10^{-9} mBar, equipped with Al $\kappa\alpha$ X-ray (1486.6 eV) was employed to analyze the oxidation state of elements in the samples. The survey scan (160 eV) with high resolution (40 eV) was used to elucidate the presence of the components and their oxidation states. The magnetic measurement was carried out in a vibrating sample magnetometer (VSM, Quantum Device PPMS Evercool II, LPCNO, INSA, Toulouse) at room temperature which identified and detailed the magnetic and coercitivity properties. The magnetic moment per formula unit (μ_{fu}) was calculated as follows:

$$\mu_{fu}(\mu_B) = \frac{M \cdot W}{\mu_B \cdot N_A} \tag{12}$$

M = magnetization in emu/g; W = molecular weight; μ_B = Bohr magneton (9.274×10^{-24} J/T); N_A = Avogadro number. Molecular weight was determined using EDS data. The Ag content in $ZnFe_2O_4$−Ag was found to be approximately 2.0% w/w.

CONCLUSIONS

AgNPs were deposited on $ZnFe_2O_4$ NPs to yield $ZnFe_2O_4$−Ag NPs. The signal for Ag was not detected in XRD until its content reached 2.5%; however, the silver particle presence in $ZnFe_2O_4$−Ag was established by TEM, HRTEM, and XPS. The existence of multiple interphases in $ZnFe_2O_4$−AgNPs is confirmed by HR-TEM, generating synergistic effects. The enhancement of the Ms values (160% times greater) for $ZnFe_2O_4$−Ag (from 7.25 to 18.71 emu/g is observed at 5.0 K as compared to 298 K. In contrast, the improvement is just about 5.0% for Fe_3O_4 (91.09 to 96.19 emu/g), illustrating that both $ZnFe_2O_4$ and $ZnFe_2O_4$−Ag are highly temperature sensitive to the magnetization. This means that these catalytic materials can be separated magnetically from the reaction medium and can be reused. A reduction of bandgap energy for $ZnFe_2O_3$−Ag is observed by the DRS spectra and it is corroborated with DOS. $ZnFe_2O_3$−Ag (2.5%) photocatalytically degrades rhodamine B ($k = 5.5 \times 10^{-3}$ min^{-1}) under visible light and follows first-order kinetics associated with photopowered adsorption (nonlinear Langmuir isotherm model). The degradation rate for $ZnFe_2O_4$ and Fe_3O_4 resulted as $k = 2.0 \times 10^{-3}$ min^{-1} and $k = 1.1 \times 10^{-3}$ min^{-1}, respectively. A greater antibacterial property for $ZnFe_2O_4$−Ag is seen by the deposition of Ag NPs on $ZnFe_2O_4$ as compared to other samples.

ASSOCIATED CONTENT

Supporting Information

The Supporting Information is available free of charge at https://pubs.acs.org/doi/10.1021/acsomega.2c03153.

Powder X-ray diffraction (PXRD), Fourier transform infrared (FT-IR) spectra, X-ray photoelectron-spectroscopy (XPS), antibacterial activity parameters, adsorption and degradation of RhB, pH effect in the photodegradation and computational studies of $ZnFe_2O_4$−Ag (PDF)

AUTHOR INFORMATION

Corresponding Author

Pandiyan Thangarasu − *Universidad Nacional Autónoma de México, Facultad de Química, Ciudad Universitaria, México City, Ciudad de México, México MX 04510;* orcid.org/0000-0001-7302-4044; Email: pandiyan@unam.mx

Authors

Carlos Alberto Huerta-Aguilar − *Instituto Tecnologico y de Estudios Superiores de Monterrey, Campus Puebla, School of Engineering and Sciences, San Andres Cholula, Puebla, México MX 72800;* orcid.org/0000-0001-9274-5330

Zarick Juliana Diaz-Puerto − *Universidad Nacional Autónoma de México, Facultad de Química, Ciudad Universitaria, México City, Ciudad de México, México MX 04510*

Eduardo Daniel Tecuapa-Flores − *Universidad Nacional Autónoma de México, Facultad de Química, Ciudad Universitaria, México City, Ciudad de México, México MX 04510*

Complete contact information is available at: https://pubs.acs.org/10.1021/acsomega.2c03153

Notes

The authors declare no competing financial interest.

ACKNOWLEDGMENTS

The authors acknowledge the Dirección General de Asuntos del Personal Académico (Project PAPIIT No IN 202622) for economic support. Research was cofounded by CAPEX Project: Renewable Energies Lab at Tecnológico de Monterrey, Puebla. The authors thank Dr. Ivan Puente, at USAI, Facultad de Química for the SEM and TEM analysis; and also Prof. Bruno Chaudret for other analytical and technical facilities including magnetic studies. The authors thank Dr Iván Jonathan Bazany Rodríguez for the EPR technical support.

REFERENCES

(1) Ghazani, A. A.; Pectasides, M.; Sharma, A.; Castro, C. M.; Mino-Kenudson, M.; Lee, H.; Shepard, J.-A. O.; Weissleder, R. Molecular characterization of scant lung tumor cells using iron-oxide nanoparticles and micro-nuclear magnetic resonance. *Nanomed. Nanotechn. Biol. Med.* **2014**, *10*, 661−668. Yokoyama, T.; Tam, J.; Kuroda, S.; Scott, A. W.; Aaron, J.; Larson, T.; Shanker, M.; Correa, A. M.; Kondo, S.; Roth, J. A.; Sokolov, K.; Ramesh, R. EGFR-Targeted Hybrid Plasmonic Magnetic Nanoparticles Synergistically Induce Autophagy and Apoptosis in Non-Small Cell Lung Cancer Cells. *PLoS One* **2011**, *6*, No. e25507. Couto, D.; Freitas, M.; Vilas-Boas, V.; Dias, I.; Porto, G.; Arturo Lopez-Quintela, M.; Rivas, J.; Freitas, P.; Carvalho, F.; Fernandes, E. Interaction of polyacrylic acid coated and

https://doi.org/10.1021/acsomega.2c03153
ACS Omega 2022, 7, 33985−34001

non-coated iron oxide nanoparticles with human neutrophils. *Toxicol. Lett.* **2014**, *225*, 57−65.
(2) Yang, H. H.; Zhang, S. Q.; Chen, X. L.; Zhuang, Z. X.; Xu, J. G.; Wang, X. R. Magnetite-containing spherical silica nanoparticles for biocatalysis and bioseparations. *Analyt. Chem.* **2004**, *76*, 1316−1321.
(3) Alivisatos, A. P. Semiconductor clusters, nanocrystals, and quantum dots. *Science* **1996**, *271*, 933−937.
(4) Cai, C.; Zhang, Z.; Liu, J.; Shan, N.; Zhang, H.; Dionysiou, D. D. Visible light-assisted heterogeneous Fenton with ZnFe2O4 for the degradation of Orange II in water. *Appl. Catal., B* **2016**, *182*, 456−468.
(5) Biswal, D.; Peeples, B. N.; Peeples, C.; Pradhan, A. K. Tuning of magnetic properties in cobalt ferrite by varying Fe+2 and Co+2 molar ratios. *J. Magn. Magn. Mater.* **2013**, *345*, 1−6. Vestal, C. R.; Song, Q.; Zhang, Z. J. Effects of interparticle interactions upon the magnetic properties of CoFe2O4 and MnFe2O4 nanocrystals. *J. Phys. Chem. B* **2004**, *108* (47), 18222−18227. Chen, L.; Shen, Y.; Bai, J. Large-scale synthesis of uniform spinel ferrite nanoparticles from hydrothermal decomposition of trinuclear heterometallic oxo-centered acetate clusters. *Mater. Lett.* **2009**, *63*, 1099−1101.
(6) Boumaza, S.; Boudjemaa, A.; Bouguelia, A.; Bouarab, R.; Trari, M. Visible light induced hydrogen evolution on new hetero-system $ZnFe_2O_4/SrTiO_3$. *Appl. Energy* **2010**, *87*, 2230−2236. Zhang, S. W.; Li, J. X.; Zeng, M. Y.; Zhao, G. X.; Xu, J. Z.; Hu, W. P.; Wang, X. K. In Situ Synthesis of Water-Soluble Magnetic Graphitic Carbon Nitride Photocatalyst and Its Synergistic Catalytic Performance. *ACS Appl. Mater. Interface* **2013**, *5*, 12735−12743.
(7) Chen, X. J.; Dai, Y. Z.; Huang, W. K. Novel $Ag_3PO_4/ZnFe_2O_4$ composite photocatalyst with enhanced visible light photocatalytic activity. *Mater. Lett.* **2015**, *145*, 125−128. Feng, J. T.; Hou, Y. H.; Wang, X. Y.; Quan, W. L.; Zhang, J. M.; Wang, Y. C.; Li, L. C. In-depth study on adsorption and photocatalytic performance of novel reduced graphene oxide-$ZnFe_2O_4$-polyaniline composites. *J. Alloys Comp.* **2016**, *681*, 157−166.
(8) Hassani, A.; Krishnan, S.; Scaria, J.; Eghbali, P.; Nidheesh, P. V. Z-scheme photocatalysts for visible-light-driven pollutants degradation: A review on recent advancements. *Current Opinion Solid State Mater. Sci.* **2021**, *25*, 100941. Hassani, A.; Eghbali, P.; Metin, O. Sonocatalytic removal of methylene blue from water solution by cobalt ferrite/mesoporous graphitic carbon nitride ($CoFe_2O_4$/mpg-C3N4) nanocomposites: response surface methodology approach. *Environ. Sci. Poll. Rsh.* **2018**, *25*, 32140−32155. Madihi-Bidgoli, S.; Asadnezhad, S.; Yaghoot-Nezhad, A.; Hassani, A. Azurobine degradation using Fe2O3@multi-walled carbon nanotube activated peroxymonosulfate (PMS) under UVA-LED irradiation: performance, mechanism and environmental application. *J. Environ. Chemical Eng.* **2021**, *9*, 106660.
(9) Rivero, M.; del Campo, A.; Mayoral, A.; Mazario, E.; Sanchez-Marcos, J.; Munoz-Bonilla, A. Synthesis and structural characterization of $ZnxFe_3$-xO_4 ferrite nanoparticles obtained by an electrochemical method. *RSC Adv.* **2016**, *6*, 40067−40076.
(10) Peng, S.; Sun, S. Synthesis and Characterization of Monodisperse Hollow Fe3O4 Nanoparticles. *Angew. Chem., Int. Ed.* **2007**, *119*, 4233−4236. Jenkins, R.; Fawcett, T. G.; Smith, D. K.; Visser, J. W.; Morris, M. C.; Frevel, L. K. JCPDS — International Centre for Diffraction Data Sample Preparation Methods in X-Ray Powder Diffraction. *Powd. Diffract.* **1986**, *1*, 51−63.
(11) Nakashima, S.; Fujita, K.; Tanaka, K.; Hirao, K.; Yamamoto, T.; Tanaka, I. First-principles XANES simulations of spinel zinc ferrite with a disordered cation distribution. *Phys. Review B* **2007**, *75*, 174443.
(12) Arulmurugan, R.; Jeyadevan, B.; Vaidyanathan, G.; Sendhilnathan, S. Effect of zinc substitution on Co-Zn and Mn-Zn ferrite nanoparticles prepared by co-precipitation. *J. Magn. Magn. Mater.* **2005**, *288*, 470−477. Jeyadevan, B.; Tohji, K.; Nakatsuka, K. Structure analysis of coprecipited ZnFe2O4 by extended x-Ray absorption fine structure. *J. Appl. Phys.* **1994**, *76*, 6325−6327.
(13) Tong, G.; Du, F.; Wu, W.; Wu, R.; Liu, F.; Liang, Y. Enhanced reactive oxygen species (ROS) yields and antibacterial activity of spongy $ZnO/ZnFe_2O_4$ hybrid micro-hexahedra selectively synthesized through a versatile glucose-engineered co-precipitation/annealing process. *J. Mater. Chem. B* **2013**, *1*, 2647−2657.
(14) Tong, G.; Liu, Y.; Wu, T.; Ye, Y.; Tong, C. High-quality elliptical iron glycolate nanosheets: selective synthesis and chemical conversion into FexOy nanorings, porous nanosheets, and nanochains with enhanced visible-light photocatalytic activity. *Nanoscale* **2015**, *7*, 16493−16503.
(15) Sertkol, M.; Köseoğlu, Y.; Baykal, A.; Kavas, H.; Bozkurt, A.; Toprak, M. S. Microwave synthesis and characterization of Zn-doped nickel ferrite nanoparticles. *J. Alloys Comp.* **2009**, *486*, 325−329. Tong, G.; Du, F.; Wu, W.; Wu, R.; Liu, F.; Liang, Y. Enhanced reactive oxygen species (ROS) yields and antibacterial activity of spongy $ZnO/ZnFe_2O_4$ hybrid micro-hexahedra selectively synthesized through a versatile glucose-engineered co-precipitation/annealing process. *J. Mater. Chem. B* **2013**, *1*, 2647−2657.
(16) Yavuz, O.; Ram, M. K.; Aldissi, M.; Poddar, P.; Hariharan, S. Synthesis and the physical properties of MnZn ferrite and NiMnZn ferrite-polyaniline nanocomposite particles. *J. Mater. Chem.* **2005**, *15*, 810−817.
(17) Kurtan, U.; Erdemi, H.; Baykal, A.; Gungunes, H. Synthesis and magneto-electrical properties of MFe_2O_4 (Co, Zn) nanoparticles by oleylamine route. *Ceram. Int.* **2016**, *42*, 13350−13358.
(18) Dehghani, F.; Hashemian, S.; Shibani, A. Effect of calcination temperature for capability of MFe2O4 (M = Co, Ni and Zn) ferrite spinel for adsorption of bromophenol red. *J. Ind. Eng. Chem.* **2017**, *48*, 36−42.
(19) Ding, C.; Zeng, Y.; Li, R.; Zhang, Y.; Zhao, L. Temperature-and time-tuned morphological evolution of polyhedral magnetite nanocrystals and their facet-dependent high-rate performance for lithium-ion batteries. *J. Alloys Comp.* **2016**, *676*, 347−355.
(20) Evdou, A.; Zaspalis, V.; Nalbandian, L. Ferrites as redox catalysts for chemical looping processes. *Fuel* **2016**, *165*, 367−378. Xu, Y.; Sun, D.; Hao, H.; Gao, D.; Sun, Y. Non-stoichiometric Co(II), Ni(II), Zn(II)-ferrite nanospheres: size controllable synthesis, excellent gas-sensing and magnetic properties. *RSC Adv.* **2016**, *6*, 98994−99002.
(21) Yuan, C.; Wu, H. B.; Xie, Y.; Lou, X. W. Mixed Transition-Metal Oxides: Design, Synthesis, and Energy-Related Applications. *Angewandte Chemie Int. Ed.* **2014**, *53*, 1488−1504.
(22) Stoeva, S. I.; Prasad, B. L. V.; Uma, S.; Stoimenov, P. K.; Zaikovski, V.; Sorensen, C. M.; Klabunde, K. J. Face-Centered Cubic and Hexagonal Closed-Packed Nanocrystal Superlattices of Gold Nanoparticles Prepared by Different Methods. *J. Phys. Chem. B* **2003**, *107*, 7441−7448.
(23) Curkovj, L.; Jelaca, M. Dissolution of alumina ceramics in HCl aqueous solution. *Ceram. Int.* **2009**, *35*, 2041−2045.
(24) Bera, S.; Prince, A.; Velmurugan, S.; Raghavan, P.; Gopalan, R.; Panneerselvam, G.; Narasimhan, S. Formation of zinc ferrite by solid-state reaction and its characterization by XRD and XPS. *J. Mater. Sci.* **2001**, *36* (22), 5379−5384.
(25) Guskos, N.; Glenis, S.; Zolnierkiewicz, G.; Typek, J.; Sibera, D.; Kaszewski, J.; Moszynski, D.; Lojkowski, W.; Narkiewicz, U. Magnetic study of Fe_2O_3/ZnO nanocomposites. *Phys. B-Conden. Mater.* **2010**, *405*, 4054−4058. Druska, P.; Steinike, U.; Sepelak, V. Surface structure of mechanically activated and of mechanosynthesized zinc ferrite. *J. Solid State Chem.* **1999**, *146*, 13−21.
(26) Aguilar, C. A. H.; Ramírez-Alejandre, A. A.; Pandiyan, T.; Arenas-Alatorre, J. A.; Reyes, I. A.; Corea, M. Crystal Phase Induced Band Gap Energy Enhancing Photo-Catalytic Properties of Zn-Fe_2O_4/Au NPs: Experimental and Theoretical studies. *Catal. Sci. Technol.* **2019**, *9*, 3066−3080.
(27) Grosvenor, A. P.; Kobe, B. A.; Biesinger, M. C.; McIntyre, N. S. Investigation of multiplet splitting of Fe 2p XPS spectra and bonding in iron compounds. *Surf. Interface Anal.* **2004**, *36*, 1564−1574. Bhosale, M. A.; Ummineni, D.; Sasaki, T.; Nishio-Hamane, D.; Bhanage, B. M. Magnetically separable gamma-Fe2O3 nanoparticles: An efficient catalyst for acylation of alcohols, phenols, and amines

https://doi.org/10.1021/acsomega.2c03153
ACS Omega 2022, 7, 33985−34001

using sonication energy under solvent free condition. *J. Mol. Catal. a-Chemical* **2015**, *404*, 8−17.
(28) Zhang, Z.; Li, W.; Zou, R.; Kang, W.; San Chui, Y.; Yuen, M. F.; Lee, C.-S.; Zhang, W. Layer-stacked cobalt ferrite (CoFe2O4) mesoporous platelets for high-performance lithium ion battery anodes. *J. Mater. Chem. A* **2015**, *3*, 6990−6997. Tan, Z.; Chua, D. H. C. ZnO Tip-Coated Carbon Nanotubes Core-Shell Structures for Photoluminescence and Electron Emission Properties. *J. Electrochem. Soc.* **2011**, *158*, K112−K116. Anandan, S.; Ohashi, N.; Miyauchi, M. ZnO-based visible-light photocatalyst Band-gap engineering and multi-electron reduction by co-catalyst. *Appl. Catal., B* **2010**, *100*, 502−509. Yousef, A.; Barakat, N. A. M.; Amna, T.; Unnithan, A. R.; Al-Deyab, S. S.; Kim, H. Y. Influence of CdO-doping on the photoluminescence properties of ZnO nanofibers: Effective visible light photocatalyst for waste water treatment. *J. Luminesc.* **2012**, *132*, 1668−1677. Ponnuvelu, D. V.; Pullithadathil, B.; Prasad, A. K.; Dhara, S.; Ashok, A.; Mohamed, K.; Tyagi, A. K.; Raja, B. Rapid synthesis and characterization of hybrid ZnO@Au core-shell nanorods for high performance, low temperature NO2 gas sensor applications. *Appl. Surf. Sci.* **2015**, *355*, 726−735.
(29) Stoner, E. C.; Wohlfarth, E. P. A mechanism of magnetic hysteresis in heterogeneous alloys. *Philosop. Transact. Royal Soc. London Ser. a-Mathemat. Phys. Sci.* **1948**, *240*, 599−642.
(30) El-Okr, M. M.; Salem, M. A.; Salim, M. S.; El-Okr, R. M.; Ashoush, M.; Talaat, H. M. Synthesis of cobalt ferrite nano-particles and their magnetic characterization. *J. Magn. Magnetic Mater.* **2011**, *323*, 920−926. Abbas, Y. M.; Mansour, S. A.; Ibrahim, M. H.; Ali, S. E. Microstructure characterization and cation distribution of nano-crystalline cobalt ferrite. *J. Magn. Magnetic Mater.* **2011**, *323*, 2748−2756.
(31) Odaci, D.; Kahveci, M. U.; Sahkulubey, E. L.; Ozdemir, C.; Uyar, T.; Timur, S.; Yagci, Y. In situ synthesis of biomolecule encapsulated gold-cross-linked poly(ethylene glycol) nanocomposite as biosensing platform: A model study. *Bioelectrochem.* **2010**, *79*, 211−217.
(32) Kubelka, P. New contributions to the optics of intensely light-scattering material. *J. Opt. Soc. Am.* **1948**, *38*, 448−457.
(33) Jeong, H. K.; Jin, M. H.; So, K. P.; Lim, S. C.; Lee, Y. H. Tailoring the characteristics of graphite oxides by different oxidation times. *J. Phys. D-Appl. Phys.* **2009**, *42*, 065418.
(34) Sutka, A.; Zavickis, J.; Mezinskis, G.; Jakovlevs, D.; Barloti, J. Ethanol monitoring by ZnFe2O4 thin film obtained by spray pyrolysis. *Sens. Act. B: Chemical* **2013**, *176*, 330−334. Singh, A.; Singh, A.; Singh, S.; Tandon, P.; Yadav, B. C.; Yadav, R. R. Synthesis, characterization and performance of zinc ferrite nanorods for room temperature sensing applications. *J. Alloys Comp.* **2015**, *618*, 475−483.
(35) Harish, K. N.; Bhojya Naik, H. S.; Prashanth kumar, P. N.; Viswanath, R. Synthesis, enhanced optical and photocatalytic study of Cd-Zn ferrites under sunlight. *Catal. Sci. Technol.* **2012**, *2*, 1033−1039.
(36) Rasalingam, S.; Peng, R.; Koodali, R. T. An insight into the adsorption and photocatalytic degradation of rhodamine B in periodic mesoporous materials. *Appl. Catal. B:Environ.* **2015**, *174*, 49−59.
(37) Sonu; Sharma, S.; Dutta, V.; Raizada, P.; Hosseini-Bandegharaei, A.; Thakur, V.; Nguyen, V. H.; VanLe, Q.; Singh, P. An overview of heterojunctioned ZnFe2O4 photocatalyst for enhanced oxidative water purification. *J. Environ. Chemical Eng.* **2021**, *9*, 105812.
(38) Oliveira, T. P.; Marques, G. N.; Macedo Castro, M. A.; Viana Costa, R. C.; Rangel, J. H. G.; Rodrigues, S. F.; dos Santos, C. C.; Oliveira, M. M. Synthesis and photocatalytic investigation of ZnFe2O4 in the degradation of organic dyes under visible light. *J. Mater. Rsc. Technol.* **2020**, *9*, 15001−15015.
(39) Li, Y.; Li, Y.; Yin, Y.; Xia, D.; Ding, H.; Ding, C.; Wu, J.; Yan, Y.; Liu, Y.; Chen, N.; Wong, P. K.; Lu, A. Facile synthesis of highly efficient ZnO/ZnFe2O4 photocatalyst using earth-abundant sphalerite and its visible light photocatalytic activity. *Appl. Catal., B* **2018**, *226*, 324−336.
(40) Huang, Y.; Zhu, D. D.; Zhang, Q.; Zhang, Y. F.; Cao, J. J.; Shen, Z. X.; Ho, W. K.; Lee, S. C. Synthesis of a Bi2O2CO3/ZnFe2O4 heterojunction with enhanced photocatalytic activity for visible light irradiation-induced NO removal. *Appl. Catal., B* **2018**, *234*, 70−78.
(41) Liu, H.; Hao, H. Y.; Xing, J.; Dong, J. J.; Zhang, Z. L.; Zheng, Z. Y.; Zhao, K. Enhanced photocatalytic capability of zinc ferrite nanotube arrays decorated with gold nanoparticles for visible light-driven photodegradation of rhodamine B. *J. Mater. Sci.* **2016**, *51*, 5872−5879.
(42) Xu, S. H.; Feng, D. L.; Shangguan, W. F. Preparations and Photocatalytic Properties of Visible-Light-Active Zinc Ferrite-Doped TiO2 Photocatalyst. *J. Phys. Chem. C* **2009**, *113*, 2463−2467.
(43) Mady, A. H.; Baynosa, M. L.; Tuma, D.; Shim, J. J. Facile microwave-assisted green synthesis of Ag-ZnFe2O4@rGO nanocomposites for efficient removal of organic dyes under UV- and visible-light irradiation. *Appl. Catal., B* **2017**, *203*, 416−427.
(44) Wu, Q.; Wang, P. F.; Niu, F. T.; Huang, C. P.; Li, Y.; Yao, W. F. A novel molecular sieve supporting material for enhancing activity and stability of Ag3PO4 photocatalyst. *Appl. Surf. Sci.* **2016**, *378*, 552−563.
(45) Liu, Y. P.; Shen, S. J.; Zhang, J. T.; Zhong, W. W.; Huang, X. H. Cu2-xSe/CdS composite photocatalyst with enhanced visible light photocatalysis activity. *Appl. Surf. Sci.* **2019**, *478*, 762−769.
(46) Li, X. J.; Tang, D. L.; Tang, F.; Zhu, Y. Y.; He, C. F.; Liu, M. H.; Lin, C. X.; Liu, Y. F. Preparation, characterization and photocatalytic activity of visible-light-driven plasmonic Ag/AgBr/$ZnFe_2O_4$ nanocomposites. *Mater. Rsc. Bulletin* **2014**, *56*, 125−133.
(47) Ichino, T.; Fessenden, R. W. Reactions of hydrated electron with various radicals: Spin factor in diffusion-controlled reactions. *J. Phys. Chem. A* **2007**, *111*, 2527−2541.
(48) Yu, K.; Yang, S.; He, H.; Sun, C.; Gu, C.; Ju, Y. Visible Light-Driven Photocatalytic Degradation of Rhodamine B over NaBiO3: Pathways and Mechanism. *J. Phys. Chem. A* **2009**, *11*, 10024−10032. Siwińska-Ciesielczyk, K.; Świgoń, D.; Rychtowski, P.; Moszyński, D.; Zgoła-Grześkowiak, A.; Jesionowski, T. The performance of multi-component oxide systems based on TiO_2, ZrO_2 and SiO_2 in the photocatalytic degradation of Rhodamine B: Mechanism and kinetic studies. *Coll. Surf. A: Physicochem. Eng. Asp.* **2020**, *586*, 124272.
(49) Al-Musawi, T. J.; Rajiv, P.; Mengelizadeh, N.; Mohammed, I. A.; Balarak, D. Development of sonophotocatalytic process for degradation of acid orange 7 dye by using titanium dioxide nanoparticles/graphene oxide nanocomposite as a catalyst. *J. Environ. Managem.* **2021**, *292*, 112777.
(50) Yilmaz, M.; Mengelizadeh, N.; Saloot, M. k.; shahbaksh, S.; Balarak, D. Facile synthesis of Fe3O4/ZnO/GO photocatalysts for decolorization of acid blue 113 under solar, visible and UV lights. *Mater. Sci. Semicond. Process.* **2022**, *144*, 106593.
(51) Al-Musawi, T. J.; Mengelizadeh, N.; Taghavi, M.; Shehu, Z.; Balarak, D. Capability of copper-nickel ferrite nanoparticles loaded onto multi-walled carbon nanotubes to degrade acid blue 113 dye in the sonophotocatalytic treatment process. *Environ. Sci. Pollut. Rsc.* **2022**, 1−14.
(52) Al-Musawi, T. J.; McKay, G.; Rajiv, P.; Mengelizadeh, N.; Balarak, D. Efficient sonophotocatalytic degradation of acid blue 113 dye using a hybrid nanocomposite of CoFe2O4 nanoparticles loaded on multi-walled carbon nanotubes. *J. Photochem. Photobiol. A: Chem.* **2022**, *424*, 113617.
(53) Borthakur, S.; Saikia, L. $ZnFe_2O_4$@ g-C3N4 nanocomposites: An efficient catalyst for Fenton-like photodegradation of environmentally pollutant Rhodamine B. *J. Environ. Chemical Eng.* **2019**, *7*, 103035.
(54) Manohar, A.; Chintagumpala, K.; Kim, K. H. Magnetic hyperthermia and photocatalytic degradation of rhodamine B dye using Zn-doped spinel Fe3O4 nanoparticles. *J. Mater. Sci.: Mater. Electron.* **2021**, *32*, 8778−8787.
(55) Zhu, B.; Cheng, H.; Ma, J.; Kong, Y.; Komarneni, S. J. C. Efficient degradation of rhodamine B by magnetically separable ZnS-ZnFe2O4 composite with the synergistic effect from persulfate. *Chemosphere* **2019**, *237*, 124547.

https://doi.org/10.1021/acsomega.2c03153
ACS Omega 2022, 7, 33985−34001

(56) Jadhav, S. A.; Khedkar, M. V.; Andhare, D. D.; Gopale, S. B.; Jadhav, K. M. Visible light photocatalytic activity of magnetically diluted Ni-Zn spinel ferrite for active degradation of rhodamine B. *Ceram. Int.* **2021**, *47*, 13980−13993.
(57) Raina, O.; Manimekalai, R. Photocatalysis of cobalt zinc ferrite nanorods under solar light. *Rsc. Chemical Int.* **2018**, *44*, 5941−5951.
(58) Balasubramanian, M.; Murali, K. R. Biosynthesis of zinc ferrite ($ZnFe_2O_4$) nanoparticles using flower extract of nyctanthes arbor-tristis and their photocatalytic activity. *Ferroelectrics* **2020**, *555*, 1−14.
(59) Jia, D.; Yu, J.; Long, S. M.; Tang, H. L. J. W. S. Technology. Novel $ZnFe_2O_4/TiO_2$/flake graphite composite as particle electrodes for efficient photoelectrocatalytic degradation of rhodamine B in water. *Water Sci. Technol.* **2018**, *2017*, 752−761.
(60) Lops, C.; Ancona, A.; Di Cesare, K.; Dumontel, B.; Garino, N.; Canavese, G.; Hérnandez, S.; Cauda, V. J. A. C. B. E. Sonophotocatalytic degradation mechanisms of Rhodamine B dye via radicals generation by micro-and nano-particles of ZnO. *Appl. Catal. B: Environ.* **2019**, *243*, 629−640.
(61) Munikrishnappa, C.; Kumar, S.; Shivakumara, S.; Rao, G. M.; Munichandraiah, N. The TiO2-graphene oxide-Hemin ternary hybrid composite material as an efficient heterogeneous catalyst for the degradation of organic contaminants. *J. Sci.: Adv. Mater. Devices* **2019**, 80−88.
(62) Bagbi, Y.; Sarswat, A.; Mohan, D.; Pandey, A.; Solanki, P. Lead and chromium adsorption from water using L-cysteine functionalized magnetite (Fe_3O_4) nanoparticles. *Sci. Repor.* **2017**, *7*, 1−15.
(63) Li, Y.; Zhang, B.-P.; Zhao, J.-X.; Ge, Z.-H.; Zhao, X.-K.; Zou, L. J. A. S. S. ZnO/carbon quantum dots heterostructure with enhanced photocatalytic properties. *Appl. Surf. Sci.* **2013**, *279*, 367−373.
(64) Mu, Z.; Hua, J.; Kumar Tammina, S.; Yang, Y. Visible light photocatalytic activity of Cu, N co-doped carbon dots/Ag3PO4 nanocomposites for neutral red under green LED radiation. *Coll. Surf. A: Physicochem. Eng. Asp.* **2019**, *578*, 123643.
(65) Liu, Y.; Yu, Y.-X.; Zhang, W.-D. J. J. o. a. compounds. Carbon quantum dots-doped CdS microspheres with enhanced photocatalytic performance. *J. Alloys Comp.* **2013**, *569*, 102−110.
(66) Sun, C.; Xu, Q.; Xie, Y.; Ling, Y.; Jiao, J.; Zhu, H.; Zhao, J.; Liu, X.; Hu, B.; Zhou, D. J. J. o. A.; et al. High-efficient one-pot synthesis of carbon quantum dots decorating Bi2MoO6 nanosheets hetero-structure with enhanced visible-light photocatalytic properties. *J. Alloys Comp.* **2017**, *723*, 333−344.
(67) Hu, Q.; Ji, M.; Di, J.; Wang, B.; Xia, J.; Zhao, Y.; Li, H. J. J. o. c. science, i. Ionic liquid-induced double regulation of carbon quantum dots modified bismuth oxychloride/bismuth oxybromide nanosheets with enhanced visible-light photocatalytic activity. *J. Colloid Interface Sci.* **2018**, *519*, 263−272.
(68) Sharma, G.; Dionysiou, D. D.; Sharma, S.; Kumar, A.; Ala'a, H.; Naushad, M.; Stadler, F. J. J. C. T. Highly efficient Sr/Ce/activated carbon bimetallic nanocomposite for photoinduced degradation of rhodamine B. *Catal. Today* **2019**, *335*, 437−451.
(69) Ahmad, M.; Rehman, W.; Khan, M. M.; Qureshi, M. T.; Gul, A.; Haq, S.; Ullah, R.; Rab, A.; Menaa, F. Phytogenic fabrication of ZnO and gold decorated ZnO nanoparticles for photocatalytic degradation of Rhodamine B. *J. Environ. Chemical Eng.* **2021**, *9*, 104725.
(70) Frisch, M. J.; Trucks, G. W.; Schlegel, H. B.; Scuseria, G. E.; Robb, M. A.; Cheeseman, J. R.; Scalmani, G.; Barone, V.; Mennucci, B.; Petersson, G. A.; Nakatsuji, H.; Caricato, M.; Li, X.; Hratchian, H. P.; Izmaylov, A. F.; Bloino, J.; Zheng, G.; Sonnenberg, J. L.; Hada, M.; Ehara, M.; Toyota, K.; Fukuda, R.; Hasegawa, J.; Ishida, M.; Nakajima, T.; Honda, Y.; Kitao, O.; Nakai, H.; Vreven, T.; Montgomery, J. A., Jr.; Peralta, J. E.; Ogliaro, F.; Bearpark, M.; Heyd, J. J.; Brothers, E.; Kudin, K. N.; Staroverov, V. N.; Kobayashi, R.; Normand, J.; Raghavachari, K.; Rendell, A.; Burant, J. C.; Iyengar, S. S.; Tomasi, J.; Cossi, M.; Rega, N.; Millam, J. M.; Klene, M.; Knox, J. E.; Cross, J. B.; Bakken, V.; Adamo, C.; Jaramillo, J.; Gomperts, R.; Stratmann, R. E.; Yazyev, O.; Austin, A. J.; Cammi, R.; Pomelli, C.; Ochterski, J. W.; Martin, R. L.; Morokuma, K.; Zakrzewski, V. G.; Voth, G. A.; Salvador, P.; Dannenberg, J. J.; Dapprich, S.; Daniels, A. D.; Farkas, O.; Foresman, J. B.; Ortiz, J. V.; Cioslowski, J.; Fox, D. J.*Gaussian 09, Gaussian Inc.; 2004 Ab Inito Molecular Orbital Theory*; John Wiley and Sons: NY, 1986.
(71) Yu, X. H.; Oganov, A. R.; Zhu, Q.; Qi, F.; Qian, G. R. The stability and unexpected chemistry of oxide clusters. *Phys. Chem. Chem. Phys.* **2018**, *20*, 30437−30444. Rohith, N. M.; Kathirvel, P.; Saravanakumar, S.; Mohan, L. Influence of Ag doping on the structural, optical, morphological and conductivity characteristics of ZnO nanorods. *Optik* **2018**, *172*, 940−952. Huerta-Aguilar, C. A.; Palos-Barba, V.; Thangarasu, P.; Koodali, R. T. Visible light driven photo-degradation of Congo red by TiO2-ZnO/Ag: DFT approach on synergetic effect on band gap energy. *Chemosphere* **2018**, *213*, 481−497.
(72) Budd, H.; Vannimenus, J. J. P. R. L. Surface forces and the jellium model. *Phys. Rev. Lett.* **1973**, *31* (19), 1218. Yu, X.; Oganov, A. R.; Zhu, Q.; Qi, F.; Qian, G. J. P. C. C. P. The stability and unexpected chemistry of oxide clusters. *Phys. Chem. Chem. Phys.* **2018**, *20*, 30437−30444.
(73) Wang, J.; Mbah, C. F.; Przybilla, T.; Apeleo Zubiri, B.; Spiecker, E.; Engel, M.; Vogel, N. Magic number colloidal clusters as minimum free energy structures. *Nat. Commun.* **2018**, *9*, 5259. Zweiback, J.; Ditmire, T.; Perry, M. D. J. O. e. Resonance in scattering and absorption from large noble gas clusters. *Optics Express.* **2000**, *6*, 236−242.
(74) Ulpe, A. C.; Bauerfeind, K. C. L.; Granone, L. I.; Arimi, A.; Megatif, L.; Dillert, R.; Warfsmann, S.; Taffa, D. H.; Wark, M.; Bahnemann, D. W.; Bredow, T. Photoelectrochemistry of Ferrites: Theoretical Predictions vs. Experimental Results. *Zeitschrift Fur Physikalische Chemie.* **2020**, *234*, 719−776.
(75) Sultan, M.; Singh, R. Magnetic and optical properties of rf-sputtered zinc ferrite thin films. *J. Appl. Phys.* **2009**, *105*, 07A512.
(76) Martin, T. P. J. P. R. *Shells of atoms. Phys. Report.* **1996**, *273* (4), 199−241. Attia, Y.; Samer, M. Metal clusters: New era of hydrogen production. *Renew. Sustain. Energy Rev.* **2017**, *79*, 878−892.
(77) Yu, J. L.; Tahmasebi, A.; Han, Y. N.; Yin, F. K.; Li, X. C. A review on water in low rank coals: The existence, interaction with coal structure and effects on coal utilization. *Fuel Process. Technol.* **2013**, *106*, 9−20.
(78) Bosetti, M.; Masse, A.; Tobin, E.; Cannas, M. Silver coated materials for external fixation devices: in vitro biocompatibility and genotoxicity. *Biomater.* **2002**, *23*, 887−892. Levard, C.; Hotze, E. M.; Lowry, G. V.; Brown, G. E., Jr. Environmental Transformations of Silver Nanoparticles: Impact on Stability and Toxicity. *Environ. Sci. Technol.* **2012**, *46*, 6900−6914. Peralta-Videa, J. R.; Zhao, L.; Lopez-Moreno, M. L.; de la Rosa, G.; Hong, J.; Gardea-Torresdey, J. L. Nanomaterials and the environment: A review for the biennium 2008−2010. *J. Hazard. Mater.* **2011**, *186*, 1−15. Rai, M. K.; Deshmukh, S. D.; Ingle, A. P.; Gade, A. K. Silver nanoparticles: the powerful nanoweapon against multidrug-resistant bacteria. *J. Appl. Microbiol.* **2012**, *112*, 841−852. Kumar, R.; Howdle, S.; Munstedt, H. Polyamide/silver antimicrobials: Effect of filler types on the silver ion release. *J. Biomed. Mater. Rsc. Part B-Appl. Biomater.* **2005**, *75B*, 311−319. Klueh, U.; Wagner, V.; Kelly, S.; Johnson, A.; Bryers, J. D. Efficacy of silver-coated fabric to prevent bacterial colonization and subsequent device-based biofilm formation. *J. Biomed. Mater. Rsc.* **2000**, *53*, 621−631.
(79) Nair, S.; Sasidharan, A.; Rani, V. V. D.; Menon, D.; Nair, S.; Manzoor, K.; Raina, S. Role of size scale of ZnO nanoparticles and microparticles on toxicity toward bacteria and osteoblast cancer cells. *J. Mater. Sci. Mater. Med.* **2009**, *20*, 235−241. Zhang, L.; Jiang, Y.; Ding, Y.; Daskalakis, N.; Jeuken, L.; Povey, M.; O'Neill, A. J.; York, D. W. Mechanistic investigation into antibacterial behaviour of suspensions of ZnO nanoparticles against E. coli. *J. Nanopart. Rsc.* **2010**, *12*, 1625−1636.
(80) Lipovsky, A.; Tzitrinovich, Z.; Friedmann, H.; Applerot, G.; Gedanken, A.; Lubart, R. EPR Study of Visible Light-Induced ROS Generation by Nanoparticles of ZnO. *J. Phys. Chem. C* **2009**, *113*, 15997−16001.

https://doi.org/10.1021/acsomega.2c03153
ACS Omega 2022, 7, 33985−34001

(81) Wahab, R.; Siddiqui, M. A.; Saquib, Q.; Dwivedi, S.; Ahmad, J.; Musarrat, J.; Al-Khedhairy, A. A.; Shin, H. S. ZnO nanoparticles induced oxidative stress and apoptosis in HepG2 and MCF-7 cancer cells and their antibacterial activity. *Coll. Surf. B-Biointerf.* **2014**, *117*, 267−276.
(82) Xing, Z.; Ju, Z.; Yang, J.; Xu, H.; Qian, Y. One-step hydrothermal synthesis of ZnFe 2 O 4 nano-octahedrons as a high capacity anode material for Li-ion batteries. *Nano Rsc.* **2012**, *5*, 477−485.
(83) Jiménez, A. B. P.; Aguilar, C. A. H.; Ramos, J. M. V.; Thangarasu, P. Synergistic Antibacterial Activity of Nanohybrid Materials ZnO-Ag and ZnO-Au: Synthesis, Characterization, and Comparative Analysis of Undoped and Doped ZnO Nanoparticles. *Aust. J. Chem.* **2015**, *68*, 288−297.
(84) Balows, A.*Manual of Clinical Microbiology*, 5th ed.; American Society for Microbiol, 1991.
(85) Coyle, M. B.*Manual of Antimicrobial Susceptibility Testing*; American Society for Microbiology, 2005.
(86) Eloff, J. N. A sensitive and quick microplate method to determine the minimal inhibitory concentration of plant extracts for bacteria. *Planta Med.* **1998**, *64*, 711−713.

https://doi.org/10.1021/acsomega.2c03153
ACS Omega 2022, 7, 33985−34001